Supplementary Information (SI) for Chemical Science.

Solvent-Free Approach for the Synthesis of Heterometallic Fe-Zn-ZIF Glass Via Melt-Quenched Process

Luis León-Alcaide[†], Celia Castillo-Blas[⊥], Vlad Martin-Diaconescu[§], Ivan Da Silva[∇], David A. Keen[∇], Thomas D. Bennett[⊥‡] and Guillermo Mínguez Espallargas*[†]

[†] Instituto de Ciencia Molecular (ICMol), Universidad de Valencia, c/ Catedrático José Beltrán, 2, 46980, Paterna, Spain

[⊥] Department of Materials Science and Metallurgy, University of Cambridge, Cambridge, CB3 0FS, United Kingdom

[§] CELLS-ALBA Synchrotron, E-08290 Cerdanyola del Vallès, Barcelona, Spain

[∇] ISIS Facility, Rutherford Appleton Laboratory, Harwell Campus, Didcot, Oxfordshire OX11 0QX, United Kingdom

[‡] Present address: School of Physical and Chemical Sciences, University of Canterbury, Private Bag 4800, Christchurch 8140, New Zealand.

Supporting Information

Contents

S1. Synthesis

All reagents were commercially available and used without further purification.

Synthesis of MUV-25(mog). A mixture of ferrocene (14 mg, 0.07 mmol), ZnO (6 mg, 0.07 mmol) and imidazole (20 mg, 0.3 mmol) were combined and sealed under vacuum in a layering tube (4 mm diameter). The mixture was heated at 150 °C for 24 hours to obtain orange crystals suitable for X-ray single-crystal diffraction. The product was allowed to cool to room temperature, and the layering tube was then opened. The unreacted precursors were extracted with acetonitrile. **MUV-25(mog)** was isolated as orange crystals. Phase purity was established by X-ray powder diffraction.

The other phases were synthesized using **MUV-25(mog)** as a precursor via different heat treatments, using a differential scanning calorimeter (DSC), see main text for details. Studies were carried out on a DSC250 instrument (TA Instruments) under a constant N_2 flow (50 $mL \cdot min^{-1}$). In all experiments a punctured capsule was used to avoid overpressure inside the capsule.

S2. Crystal structures

S2.1. Crystallographic information

Single crystals of **MUV-25(mog)** and **MUV-25(zni)** were mounted on glass fibers using a viscous hydrocarbon oil to coat the crystals and then transferred directly to the cold nitrogen stream for data collection. X-ray data were collected at 120 K on a DW rotating anode synergy Rigaku diffractometer with a Cu-K_{α} X-ray source (λ = 1.54184Å). Data were measured using the CrysAlisPro suite of programs.

Crystal structure determinations and refinements. The program CrysAlisPro, Rigaku, was used for unit cell determinations and data reduction. An empirical absorption correction was performed using spherical harmonics, implemented in the SCALE3 ABSPACK scaling algorithm, based upon symmetry-equivalent reflections combined with measurements at different azimuthal angles. The crystal structures were solved and refined against all F^2 values using the SHELXL and Olex2 suite of programs.[1,2] Atomic displacement parameters of all nonhydrogen atoms were refined anisotropically. Hydrogen atoms were placed in calculated positions, refined using idealized geometries (riding model) and assigned fixed isotropic displacement parameters.

CCDC 2373266 – 2373267 contain the supplementary crystallographic data for this paper. These data can be obtained free of charge via www.ccdc.cam.ac.uk/conts/retrieving.html (or from the Cambridge Crystallographic Data Centre, 12 Union Road, Cambridge CB21EZ, UK; fax: (+44)1223-336-033; or deposit@ccdc.cam.ac.uk).

Table S1. Crystallographic information of compounds **MUV-25(mog)** and **MUV-25(zni)**

Identification code	**MUV-25(mog)**	**MUV-25(zni)**
Empirical formula	$C_{24}H_{26}N_{16}FeZn_2$	$C_{12}H_{12}N_8Fe_{0.67}Zn_{1.33}$
Formula weight	725.20	392.69
Temperature/K	120(2)	120(2)
Crystal system	monoclinic	tetragonal
Space group	$P2_1/c$	$I4_1cd$
a/Å	10.38840(10)	23.4527(4)
b/Å	13.2702(2)	23.4527(4)
c/Å	10.44280(10)	12.5316(4)
α/°	90	90
β/°	92.5540(10)	90
γ/°	90	90
Volume/Å^3	1438.17(3)	6892.7(3)
Z	2	16
ρ_{calc}/g·cm^{-3}	1.675	1.514
μ/mm^{-1}	6.331	6.854
F(000)	736.0	3157.0
Crystal size/mm^3	0.08 × 0.06 × 0.03	0.08 × 0.05 × 0.05
Radiation	Cu K_α (λ = 1.54184)	Cu K_α (λ = 1.54184)
2Θ range for data collection/°	8.52 to 156.786	7.538 to 156.308
Index ranges	$-13 \le h \le 13$, $-15 \le k \le 16$, $-13 \le l \le 13$	$-24 \le h \le 29$, $-29 \le k \le 29$, $-15 \le l \le 15$
Reflections collected	28704	34407
Independent reflections	3054 [R_{int} = 0.0307, R_{sigma} = 0.0152]	3653 [R_{int} = 0.1000, R_{sigma} = 0.0441]
Data/restraints/parameters	3054/0/196	3653/1/200
Goodness-of-fit on F^2	1.108	0.986
Final R indexes [I>=2σ (I)]	R_1 = 0.0265 wR_2 = 0.0704	R_1 = 0.0417 wR_2 = 0.1098
Final R indexes [all data]	R_1 = 0.0288 wR_2 = 0.0760	R_1 = 0.0544 wR_2 = 0.1199
Largest diff. peak/hole / e Å^{-3}	0.33/–0.49	0.34/–0.46

S2.2. Structural parameters of IMIDFE, OWIGIL and MUV-25

Table S2. Selected crystallographic parameters of **IMIDFE**, **OWIGIL** and **MUV-25.**

Identification code	**IMIDFE**	**OWIGIL**	**MUV-25**
Space group	$P2_1/c$	$P2_1/c$	$P2_1/c$
Formula	$C_{24}H_{26}N_{16}Fe_3$	$C_{24}H_{26}N_{16}Co_3$	$C_{24}H_{26}N_{16}Fe_1Zn_2$
a/Å	10.516(2)	10.324(2)	10.3884(1)
b/Å	12.914(2)	13.256(3)	13.2702(2)
c/Å	10.588(2)	10.426(2)	10.4428(1)
α/°	90	90	90
β/°	92.79(3)	92.36(3)	92.554(1)
γ/°	90	90	90
Volume/Å^3	1436.18	1425.64	1438.17
Temperature (K)	283	173	120

Table S3. Refinement parameters for **MUV-25** under various configurations in which the tetrahedral and octahedral positions are refined as Fe or Zn. The best refinement is obtained when the tetrahedral position is refined as Zn and the octahedral position is refined as Fe.

	Fe_{Td}–Fe_{Oh}	**Zn_{Td}–Zn_{Oh}**	**Fe_{Td}–Zn_{Oh}**	**Zn_{Td}–Fe_{Oh}**
Goodness-of-fit on F^2	1.085	1.149	1.098	1.109
Final R indexes [I>=2σ (I)]	$R_1 = 0.0479$, $wR_2 = 0.1282$	$R_1 = 0.0462$, $wR_2 = 0.1256$	$R_1 = 0.0728$, $wR_2 = 0.1997$	$R_1 = 0.0265$, $wR_2 = 0.0704$
Final R indexes [all data]	$R_1 = 0.0512$, $wR_2 = 0.1337$	$R_1 = 0.0487$, $wR_2 = 0.1283$	$R_1 = 0.0767$, $wR_2 = 0.2050$	$R_1 = 0.0288$, $wR_2 = 0.0760$
Largest diff. peak/hole / e Å^{-3}	1.25/–1.17	0.46/–1.88	2.27/–2.72	0.33/–0.49

Table S4. Refinement parameters for **MUV-25(zni)** under various configurations, characterized by two distinct tetrahedral positions, labeled as position A and position B. The options include: using only Fe in position A and Zn in A and B; only Fe in position B and Zn in A and B; Fe and Zn in position A and B; only Zn; and only Fe. The total ratio Fe:Zn is maintained as 1:2 in all the heterometallic refinements. The best refinement is obtained with a random distribution of the Fe and Zn atoms in the two positions.

	$0.33Fe_A$-$0.66Zn_A$ $0.33Fe_B$-$0.66Zn_B$	**$0.66Fe_A$-$0.33Zn_A$ $1Zn_B$**	**$1Zn_A$ $0.66Fe_B$-$0.33Zn_B$**	**$1Fe_A$ $1Fe_B$**	**$1Zn_A$ $1Zn_B$**
Goodness-of-fit on F^2	0.986	1.132	1.036	1.042	1.042
Final R indexes [I>=2σ (I)]	$R_1 = 0.0417$ $wR_2 = 0.1098$	$R_1 = 0.0442$ $wR_2 = 0.1149$	$R_1 = 0.0451$ $wR_2 = 0.1155$	$R_1 = 0.0465$, $wR_2 = 0.1184$	$R_1 = 0.0442$ $wR_2 = 0.1157$
Final R indexes [all data]	$R_1 = 0.0544$ $wR_2 = 0.1199$	$R_1 = 0.0576$ $wR_2 = 0.1247$	$R_1 = 0.0585$, $wR_2 = 0.1256$	$R_1 = 0.0598$, $wR_2 = 0.1292$	$R_1 = 0.0569$, $wR_2 = 0.1252$
Largest diff. peak/hole / $eÅ^{-3}$	0.34/–0.46	0.37/–0.54	0.40/–0.55	0.40/–0.42	0.41/–0.52

S3. X-ray powder diffraction

All materials were characterized by X-ray powder diffraction. The samples were lightly ground in an agate mortar and pestle and used to fill 0.7 mm borosilicate capillaries that were mounted and aligned on an Empyrean PANalytical powder diffractometer, using Cu Kα radiation (λ = 1.54056Å).

S3.1. Synthesis conditions

The nomenclature used in this section corresponds to the synthetic amounts of iron and zinc precursors used during the synthesis. For example, 40Zn:60Fe indicates the phases obtained using 40% zinc oxide and 60% ferrocene. Similarly, 50Zn:50Fe and 60Zn:40Fe correspond to phases obtained using 50% zinc oxide with 50% ferrocene, and 60% zinc oxide with 40% ferrocene, respectively. The different graphs presented in this section correspond to variations in synthesis protocols, including modifications in temperature and reaction time.

Multiple phases can appear depending on synthetic parameters and the ratio of metal precursors. These phases are **IMIDFE** (pure iron), **KUMXEW** (pure zinc), **ZIF-zni** (pure zinc) or **MUV-25(mog)** (zinc and iron). To elucidate the distinct phases achievable through solvent-free methodology, we conducted a thorough investigation altering synthetic conditions to achieve pure **MUV-25(mog)**. We demonstrate that optimal conditions for obtaining pure **MUV-25(mog)** entail a temperature of 150 ºC for 24 hours, employing an equimolar ratio of 1:1 for each metal precursor.

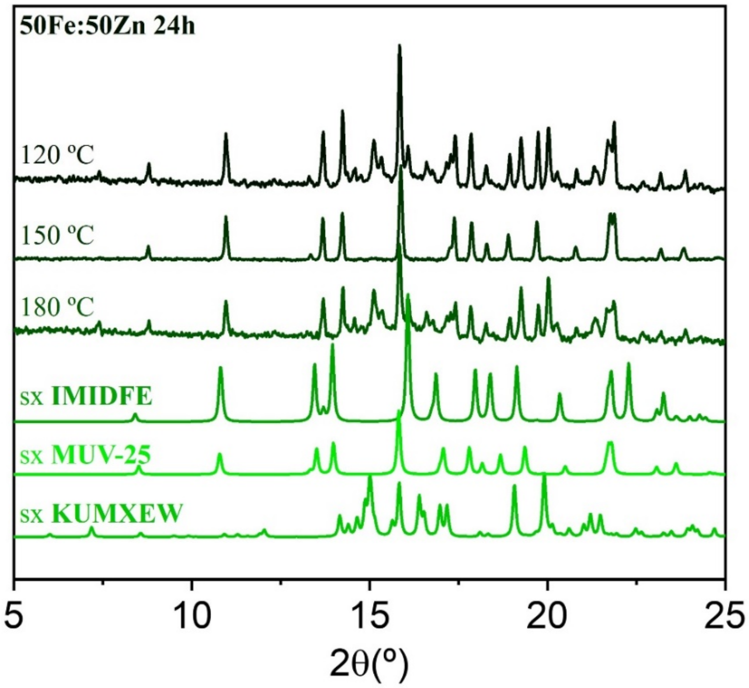

Figure S1. X-ray powder diffraction was performed on 50Zn:50Fe samples synthesized at temperatures of 120 ºC, 150 ºC, and 180 ºC over a 24-hour period. **IMIDFE** and **KUMXEW** represent the theoretical diffraction patterns of the pure iron and zinc phases, respectively. Additionally, **MUV-25(mog)** is identified as the unique phase able of incorporating both metals within the same network.

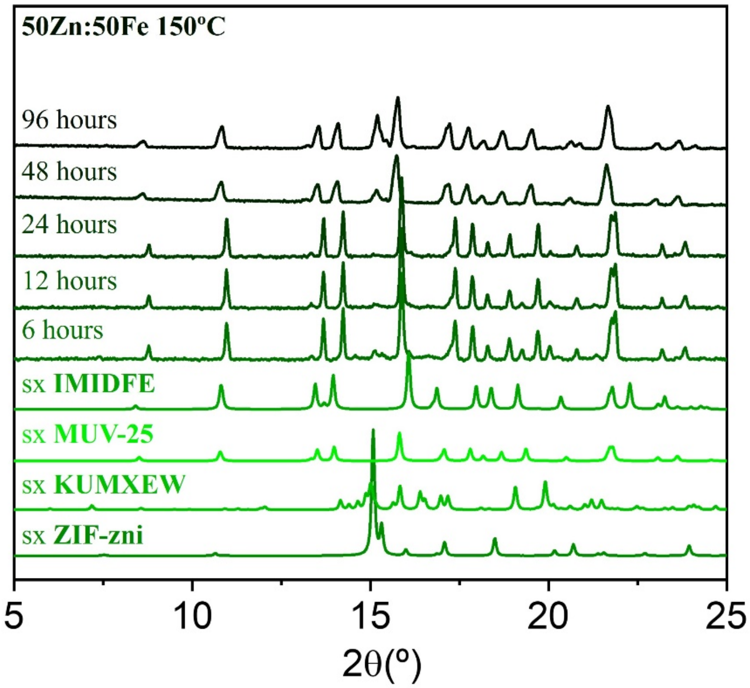

Figure S2. X-ray powder diffraction was performed on 50Zn:50Fe samples synthesized at 150ºC for intervals of 6 hours, 12 hours, 24 hours, 48 hours, and 96 hours. **IMIDFE, KUMXEW** and **ZIF-zni** represent the theoretical diffraction patterns of the pure iron and zinc phases, respectively. Additionally, **MUV-25(mog)** is identified as the unique phase able of incorporating both metals within the same network.

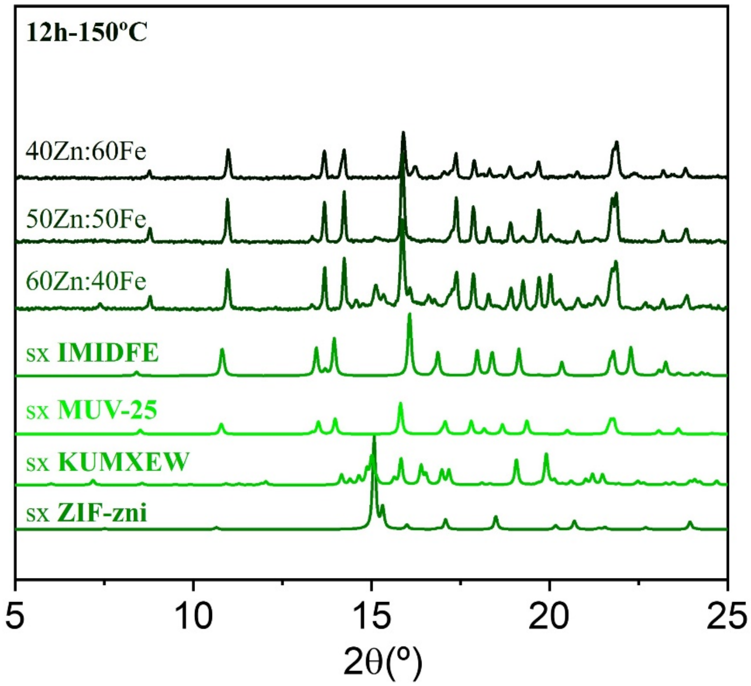

Figure S3. X-ray powder diffraction was performed on samples of 60Zn:40Fe, 50Zn:50Fe and 40Zn:60Fe synthesized at 150 ºC for 12 hours. **IMIDFE, KUMXEW** and **ZIF-zni** represent the theoretical diffraction patterns of the pure iron and zinc phases, respectively. Additionally, **MUV-25(mog)** is identified as the unique phase able of incorporating both metals within the same network.

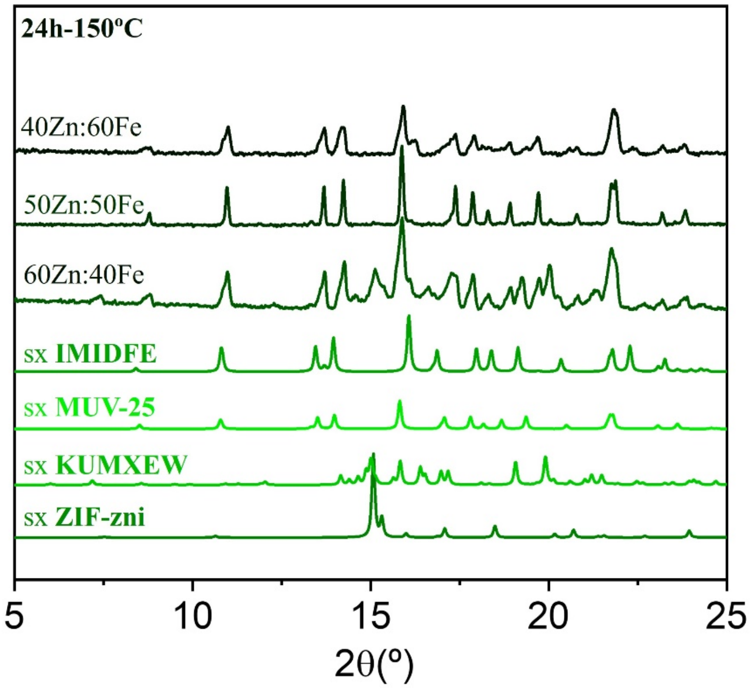

Figure S4. X-ray powder diffraction was performed on samples of 60Zn:40Fe, 50Zn:50Fe and 40Zn:60Fe synthesized at 150 ºC for 24 hours. **IMIDFE, KUMXEW** and **ZIF-zni** represent the theoretical diffraction patterns of the pure iron and zinc phases, respectively. Additionally, **MUV-25(mog)** is identified as the unique phase able of incorporating both metals within the same network.

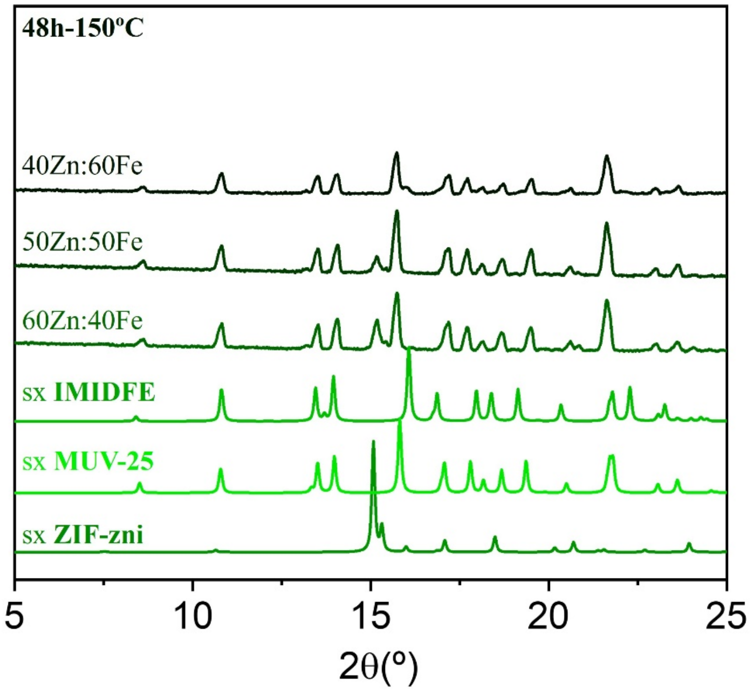

Figure S5. X-ray powder diffraction was performed on samples of 60Zn:40Fe, 50Zn:50Fe and 40Zn:60Fe synthesized at 150 ºC for 48 hours. **IMIDFE** and **ZIF-zni** represent the theoretical diffraction patterns of the pure iron and zinc phases, respectively. Additionally, **MUV-25(mog)** is identified as the unique phase able of incorporating both metals within the same network.

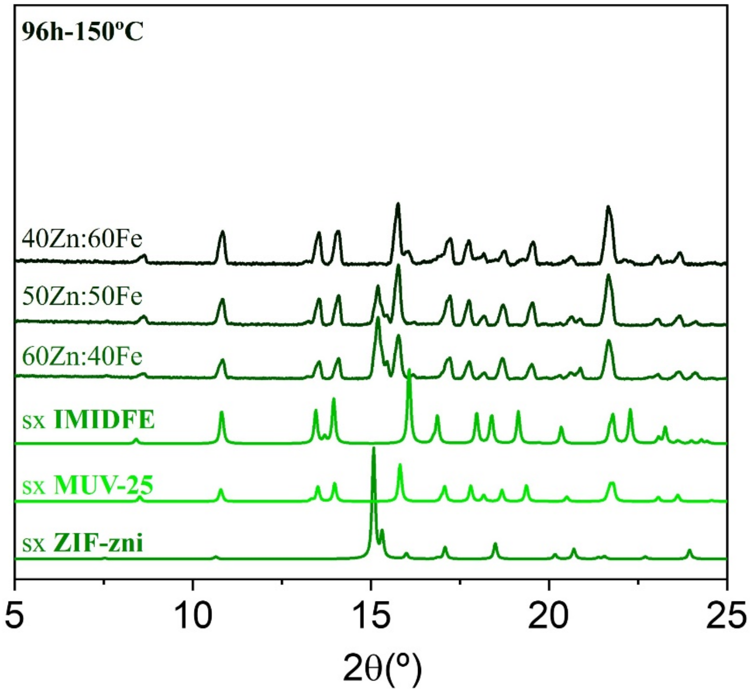

Figure S6. X-ray powder diffraction was performed on samples of 60Zn:40Fe, 50Zn:50Fe and 40Zn:60Fe synthesized at 150 ºC for 48 hours. **IMIDFE** and **ZIF-zni** represent the theoretical diffraction patterns of the pure iron and zinc phases, respectively. Additionally, **MUV-25(mog)** is identified as the unique phase able of incorporating both metals within the same network.

S3.2. Phase purity

Topas Academic v6 software was used for the Rietveld refinement procedure; the crystal structure obtained from the single crystal X-ray diffraction experiment was used as structural model for **MUV-25(mog)**, while structural data for **IMIDFE** and **KUMXEW** were downloaded from the CCDC database. During refinements, the cell parameters were the only structural parameters refined for each crystalline phase.

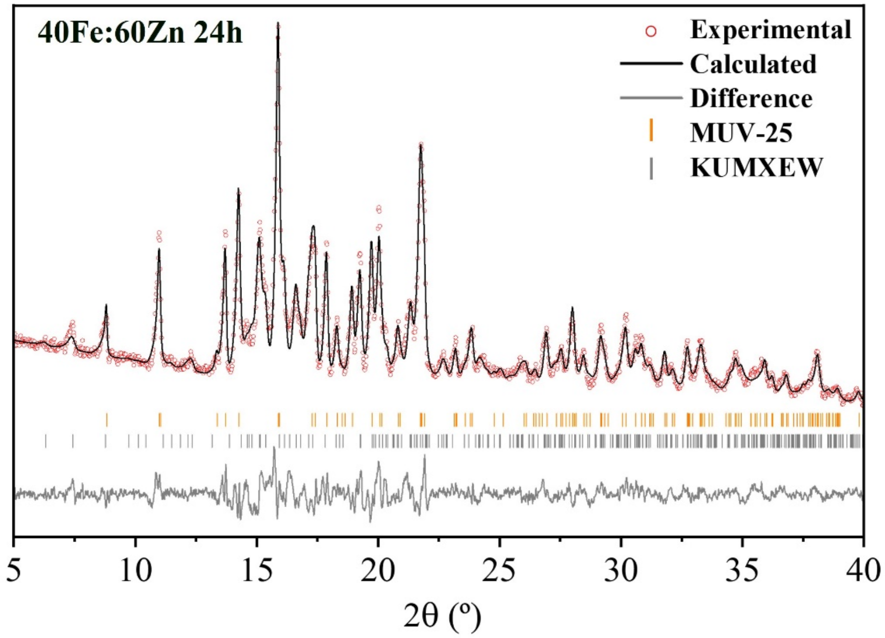

Figure S7. Experimental (red dots), calculated (black line), difference (grey line) and Bragg positions of **MUV-25(mog)** and **KUMXEW** (ticks). The calculated weight percentages are 53.72% **MUV-25(mog)** and 46.28% **KUMXEW**. R_{wp} = 16.03%.

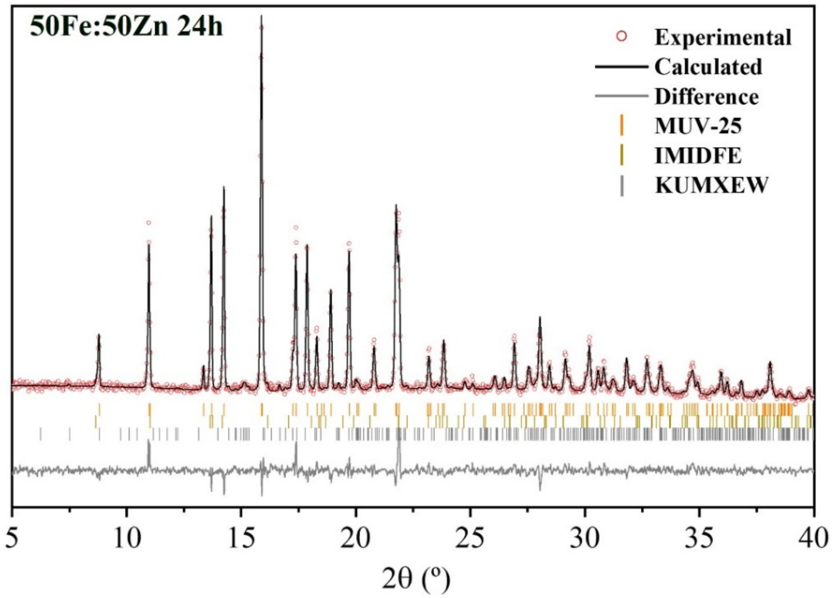

Figure S8. Experimental (red dots), calculated (black line), difference (grey line) and Bragg positions of **MUV-25(mog)**, **IMIDFE** and **KUMXEW** (ticks). The calculated weight percentages are 92.74% **MUV-25(mog)**, 1.93% **IMIDFE**, and 5.33% **KUMXEW**. R_{wp} = 17.27%.

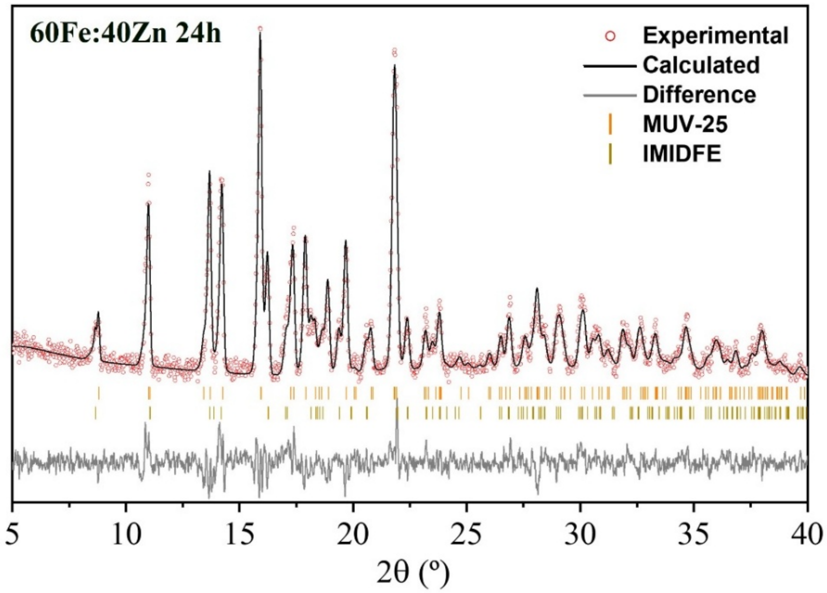

Figure S9. Experimental (red dots), calculated (black line), difference (grey line) and Bragg positions of **MUV-25(mog)**, and **IMIDFE** (ticks). The calculated weight percentages are 75.79% **MUV-25(mog)** and 24.21% **IMIDFE**. R_{wp} = 20.74%.

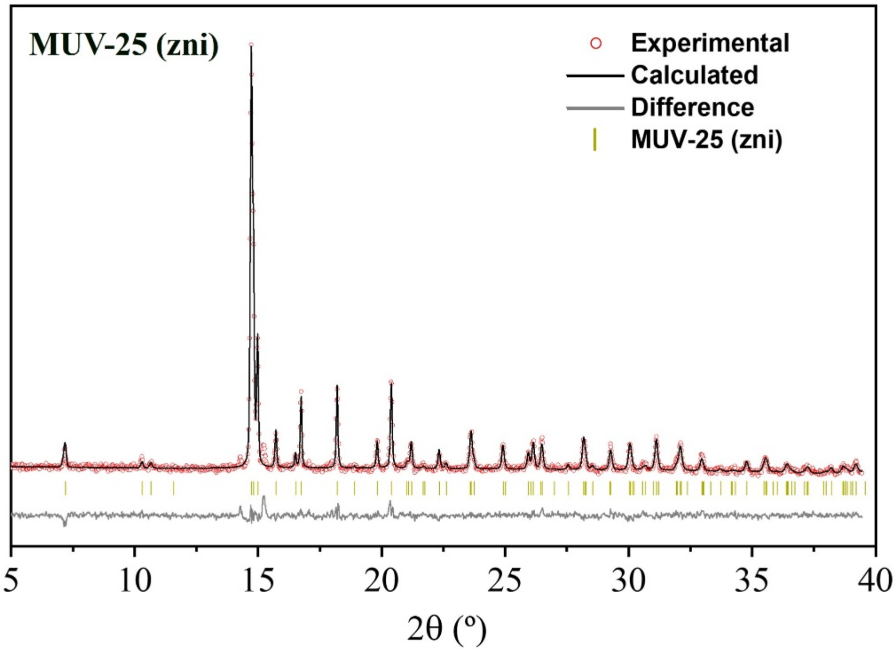

Figure S10. Experimental (red dots), calculated (black line), difference (grey line) and Bragg positions of **MUV-25(zni)** (ticks). R_{wp} = 12.77%.

S3.3. Stability tests

Crystals of **MUV-25(mog)** were exposed to air under ambient conditions for variable durations. Subsequently, the materials underwent examination via X-ray powder diffraction. For **MUV-25(mog)** the diffraction peaks remained consistent with those observed prior to air exposure. However, in the case of the **MUV-25(zni)** a decrease in peak intensity was observed.

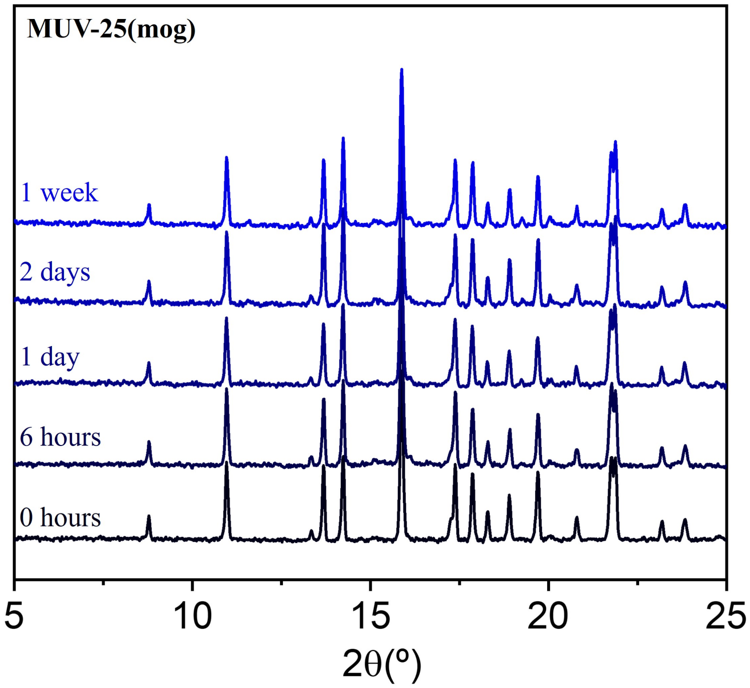

Figure S11. Powder X-ray diffraction of **MUV-25(mog)** at different times in air atmosphere to study its stability.

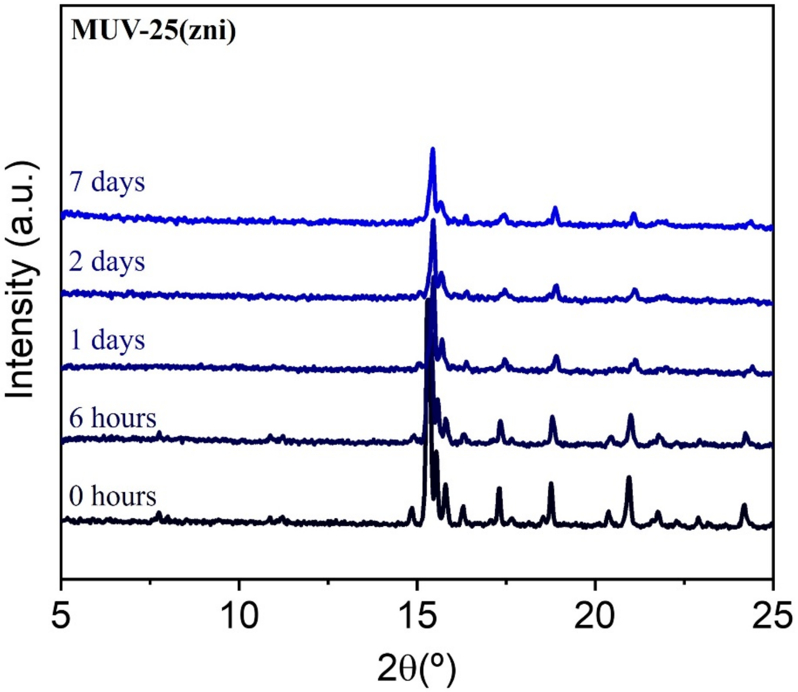

Figure S12. Powder X-ray diffraction of **MUV-25(zni)** at different times in air atmosphere to study its stability

S3.4. Pure phases (IMIDFE and KUMXEW)

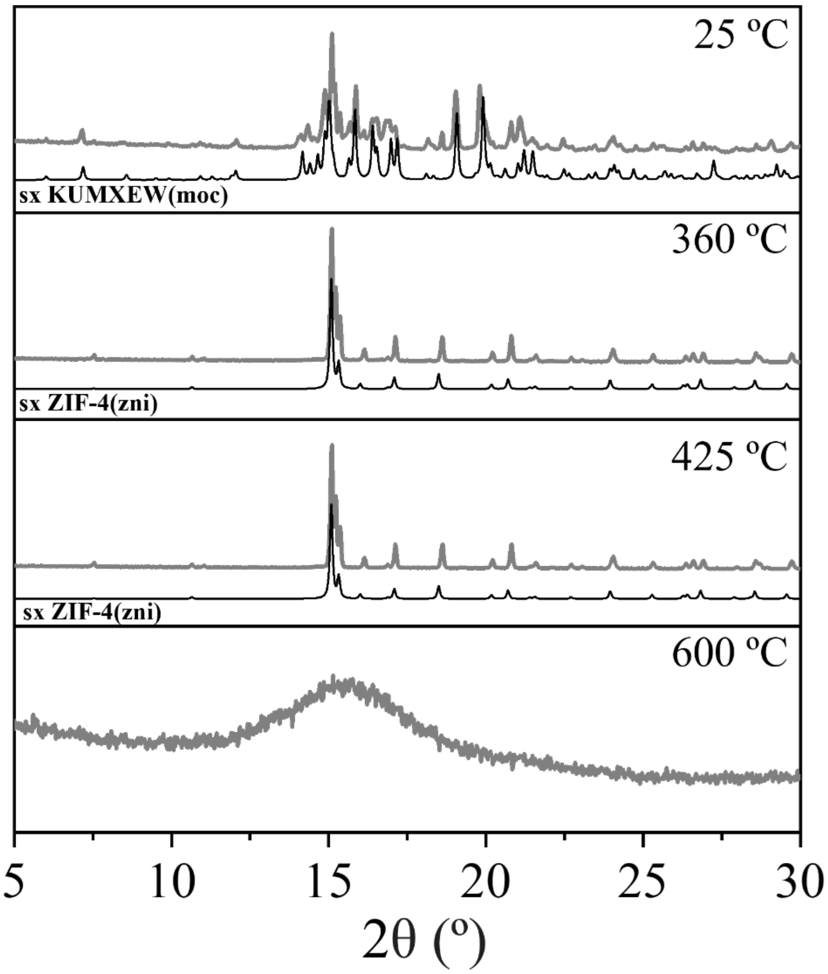

Figure S13. X-ray powder diffraction patterns of **KUMXEW** after heating and cooling at 25 ºC, 360 ºC, 425 ºC, and 600 ºC at a rate of 10 ºC min^{-1}. The grey lines represent the experimental patterns, while the black lines correspond to the theoretical powder patterns of each phase.

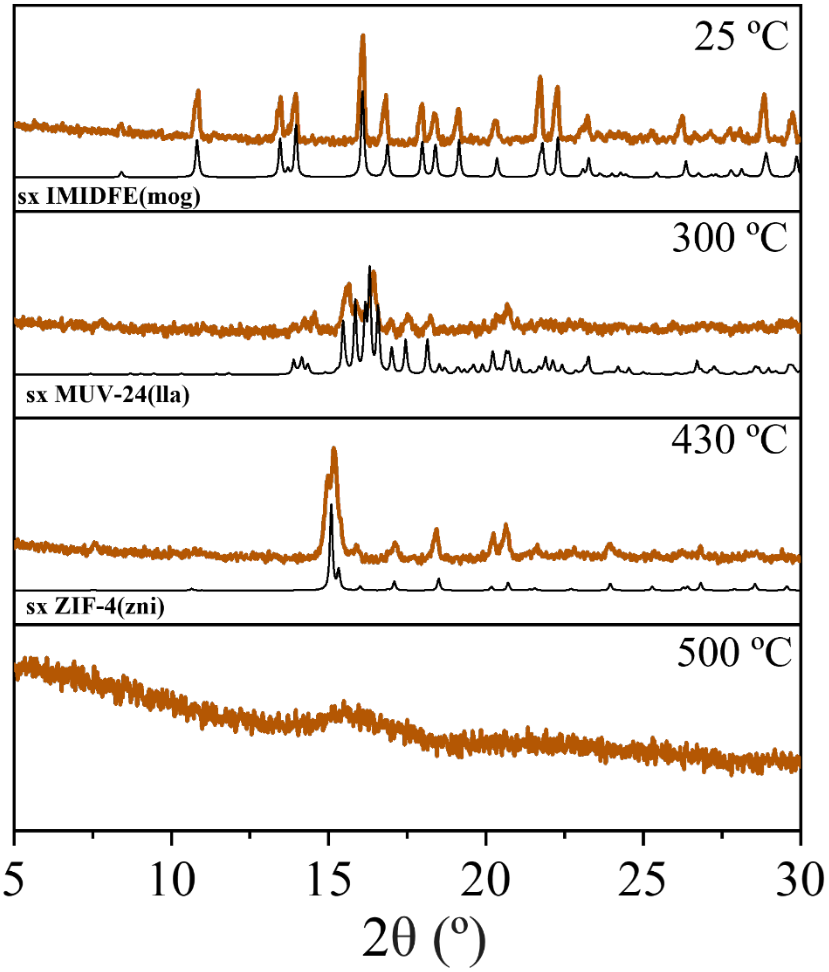

Figure S14. X-ray powder diffraction patterns of **IMIDFE** after heating and cooling at 25 ºC, 300 ºC, 430 ºC, and 500 ºC at a rate of 10ºC min^{-1}. The grey lines represent the experimental patterns, while the black lines correspond to the theoretical powder patterns of each phase.

S4. X-ray total scattering

X-ray total scattering data were collected at beamline I15-1, Diamond Light Source, UK (EE200338). All powdered samples were ground and loaded into kapton® capillaries (1 mm diameter) to a height of 0.5 cm. The capillaries were sealed with plasticine in both ends and a stainless steel rod was placed inside the empty section of capillary to provide rigidity before being mounted onto the beamline. Total scattering data were collected at room temperature for the background (*i.e.*, empty instrument), empty kapton capillary, and for all samples in a *Q* range of 0.2–22.0 $Å^{-1}$ ($\lambda = 0.161669$ Å, 76.69 keV). The total scattering data were processed to account for absorption corrections and various scattering corrections including background scattering, multiple scattering, container scattering, and Compton scattering, in a *Q* range of 0.35–20.0 $Å^{-1}$. Subsequent Fourier transformations of the processed total scattering data resulted in a real-space PDF *G(r)* and *D(r)* for each material. In this work, we use the *D(r)* form of the PDF to accentuate high *r* correlations. All processing of the total scattering data was performed using GudrunX following well-documented procedures.[3-5]

Calculated pair distribution functions (*g*(r)s) have been performed using PDFGUI.[6] This PDF function is equivalent to the employed *D*(r).[5] Anisotropy parameters were modified to 0.005 and 0.001 to observe all the correlations.

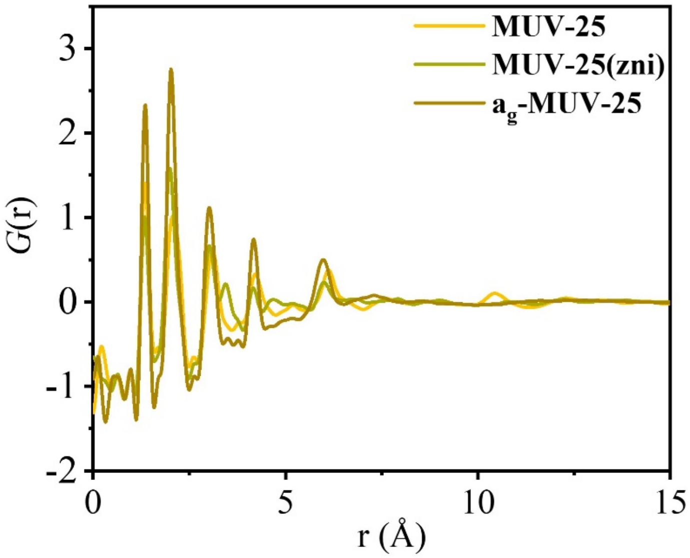

Figure S15. X-ray PDF in the form of *G*(r) of **MUV-25**, **MUV-25(zni)** and **a_g-MUV-25**.

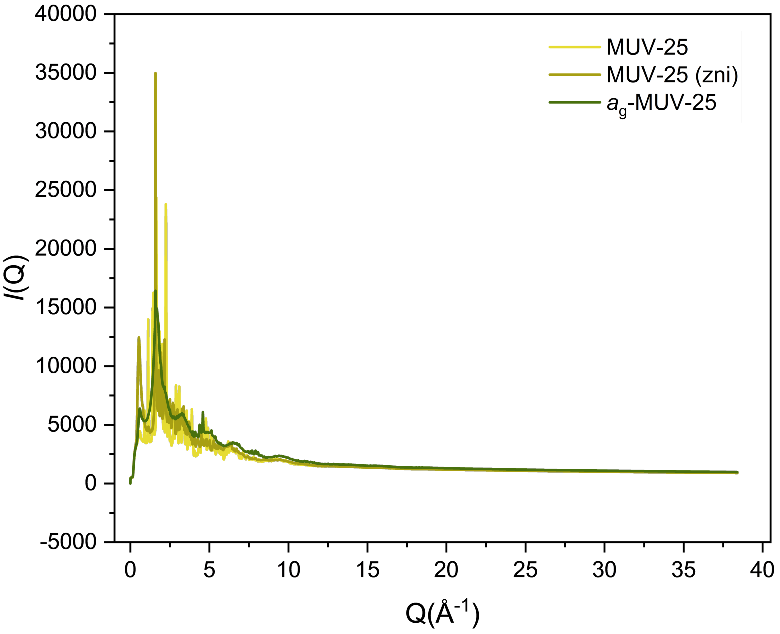

Figure S16. X-ray total scattering data of **MUV-25**, **MUV-25(zni)** and **a_g-MUV-25** (λ = 0.161669 Å, 76.69 keV).

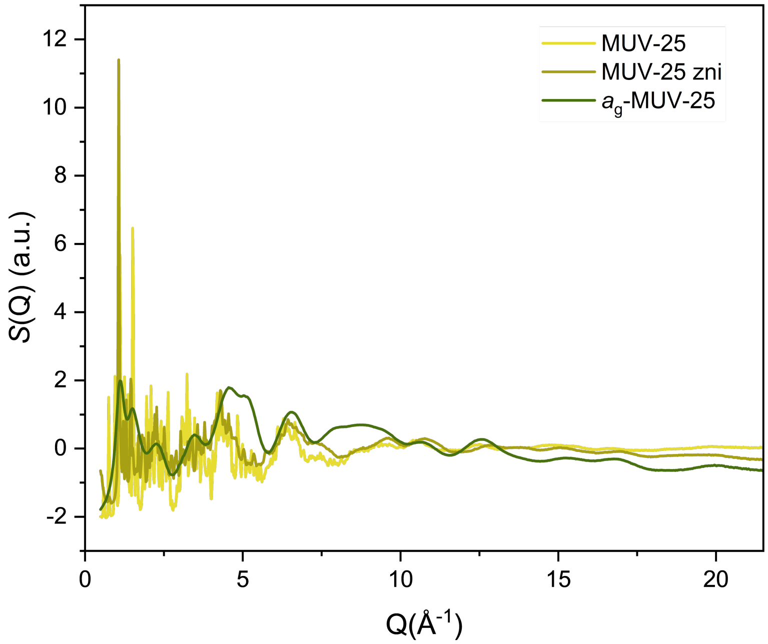

Figure S17. Total scattering structure factors, *S*(Q), of **MUV-25**, **MUV-25(zni)** and **a_g-MUV-25**.

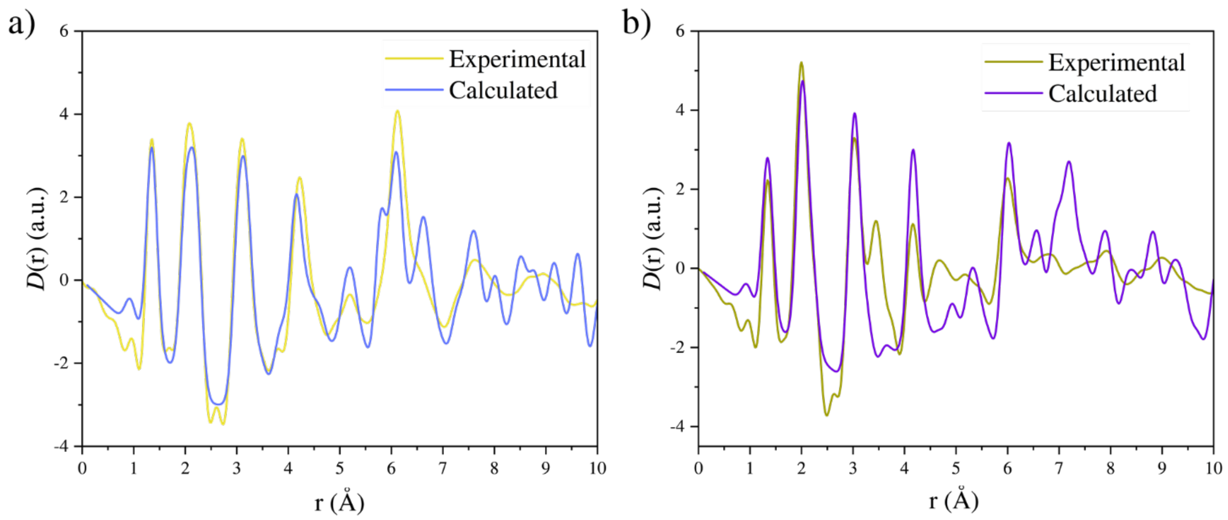

Figure S18. Experimental PDF functions compared with calculated PDFs based on their crystal structures using PDFGui for a) **MUV-25(mog)** and b) **MUV-25(zni)**. The pair correlations for **MUV-25** are mainly the same, but for **MUV-25(zni)** there are additional peaks in the experimental data.

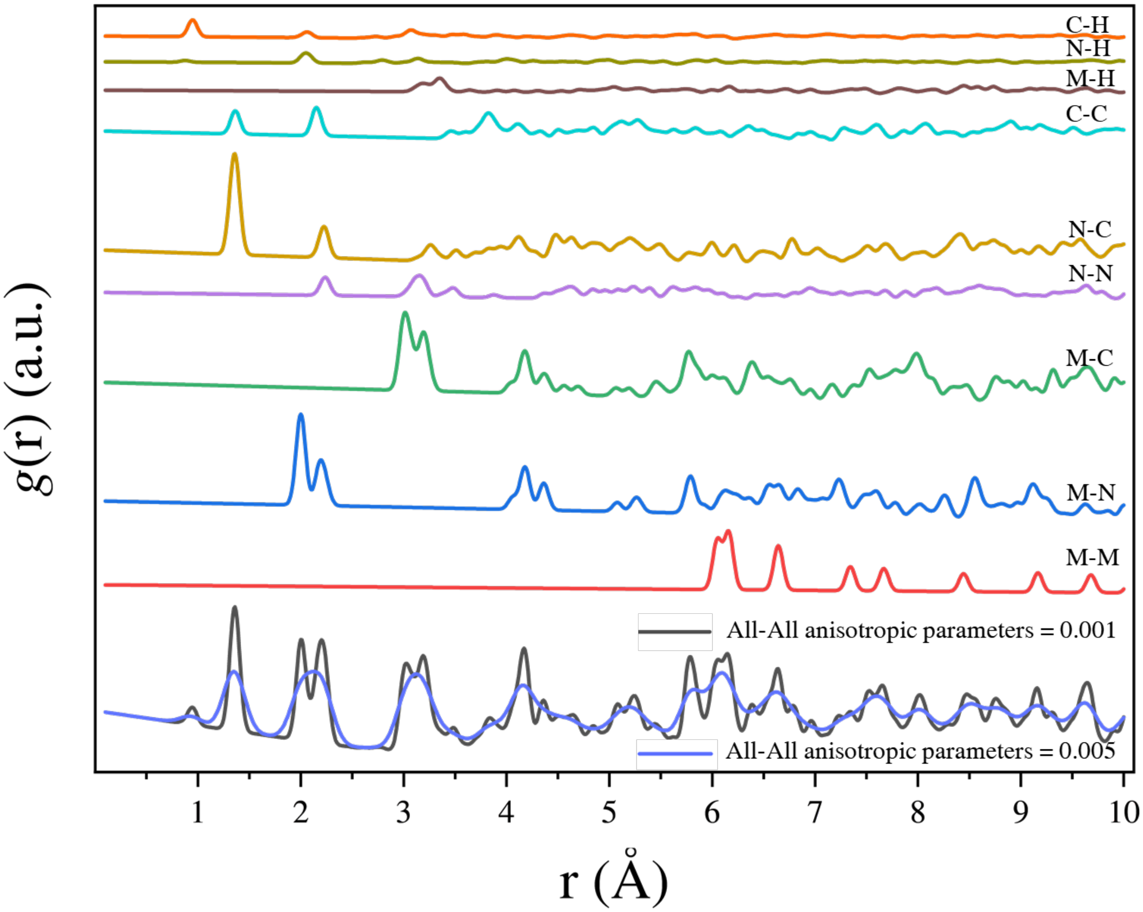

Figure S19. Calculated partial PDFs of **MUV-25(mog)** for all the correlations depicted with a single fixed value of anisotropic displacement parameter of 0.001 to show the different contributions from the different metals (M = Zn, Fe). Calculated PDFs are compared using 0.005 and 0.001 anisotropic parameters. H-H correlations are omitted because they have an extremely low contribution to the PDF.

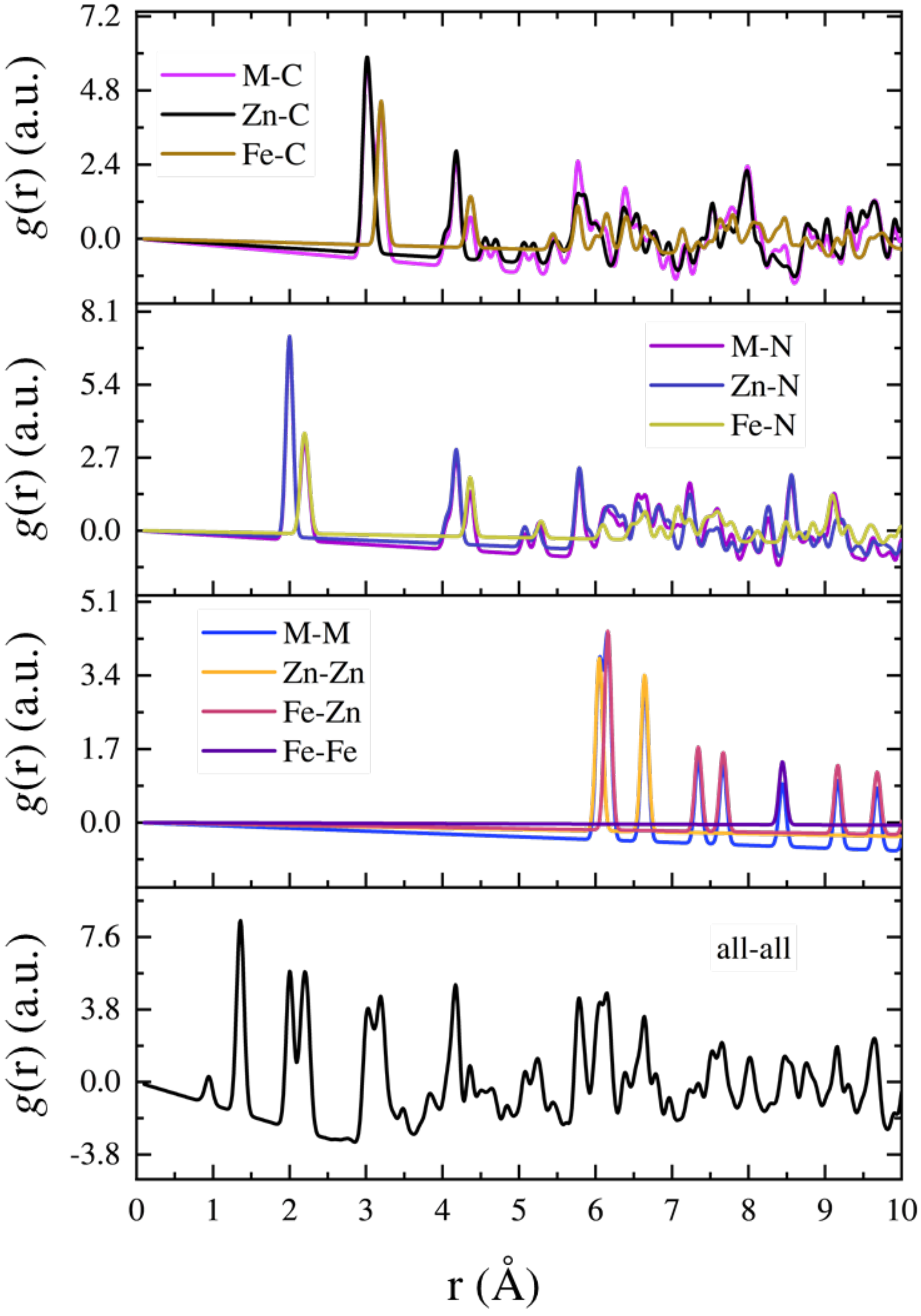

Figure S20. Partial PDFs of **MUV-25(mog)** showing the differences between Zn and Fe correlations.

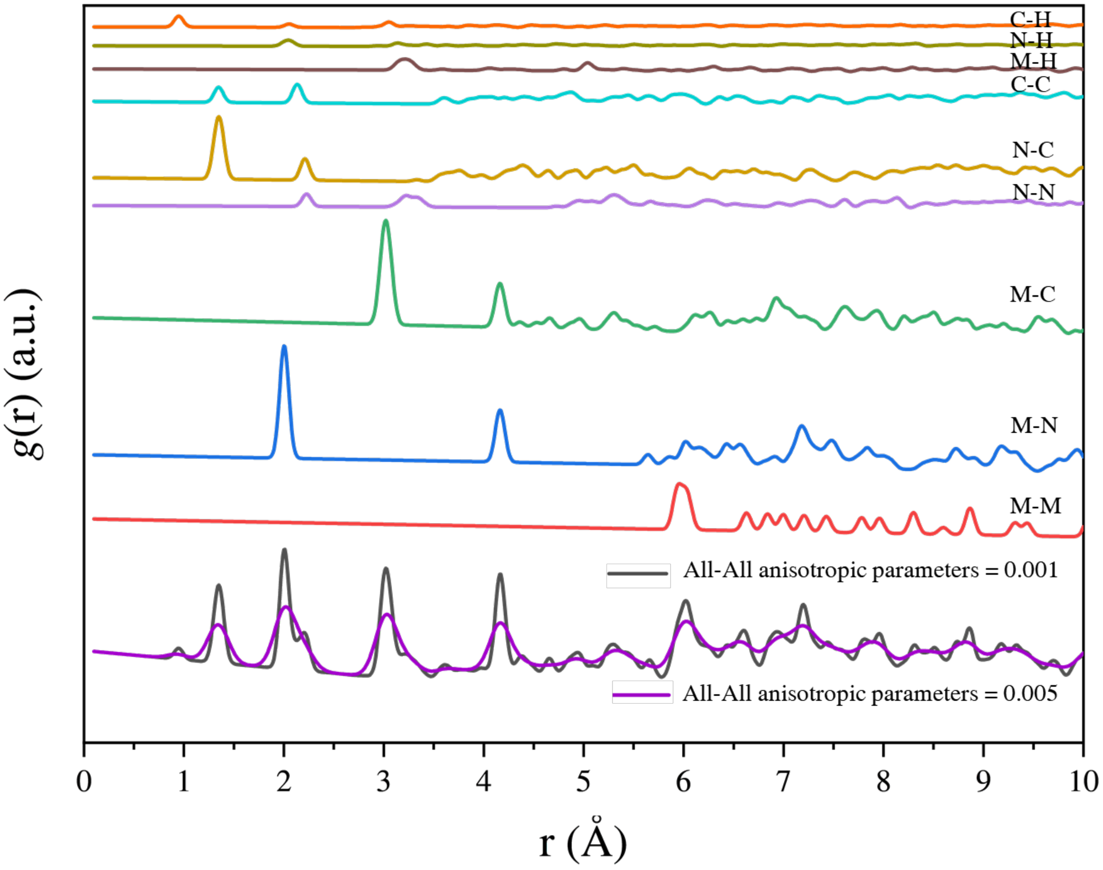

Figure S21. Calculated partial PDFs of **MUV-25(zni)** for all the correlations depicted with a single fixed value of anisotropic displacement parameter of 0.001 to show the different contributions from the different metals (M = Zn, Fe). Calculated PDFs are compared using 0.005 and 0.001 anisotropic parameters. H–H correlations are omitted because they have an extremely low contribution to the PDF. Zn and Fe occupy the same atomic positions with partial occupations in the average crystal structure, therefore they cannot be distinguished in this calculated PDF.

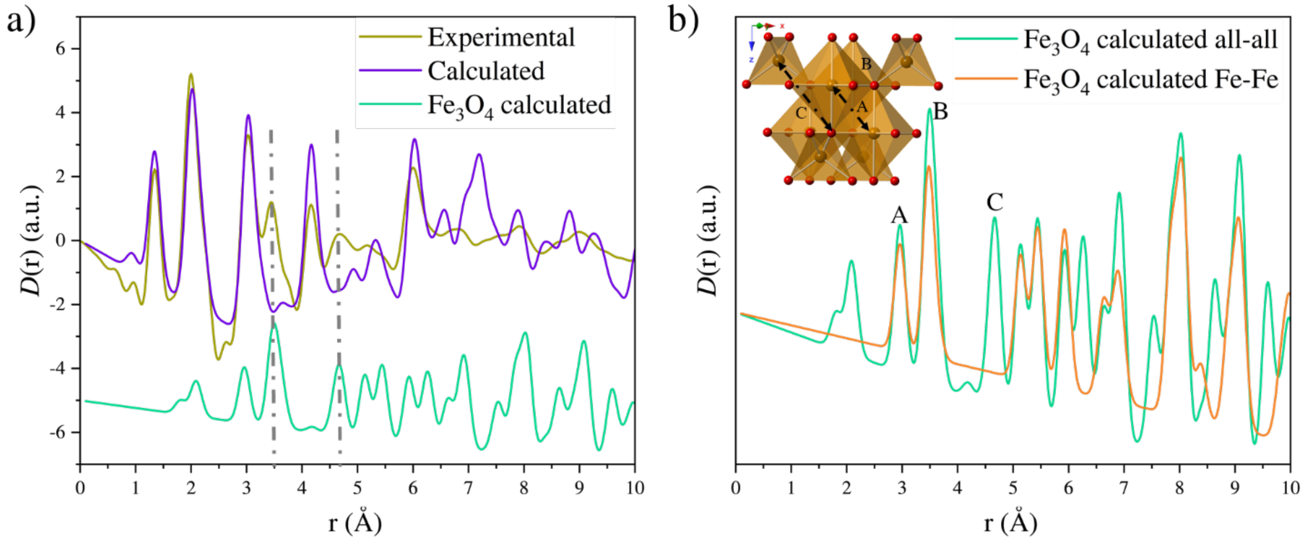

Figure S22. a) Comparison of the experimental and calculated PDFs of **MUV-25(zni)** with the calculated PDF for Fe_3O_4 (spinel structure).[7] b) Calculated Fe–Fe partial PDF and total PDF for the Fe_3O_4 to show the main Fe–Fe correlations of this structure.

S5. X-ray absorption spectroscopy

Spectra were collected on **MUV-25**, **MUV-25(zni)** and **a$_g$-MUV-25** at both the Zn and Fe K-edge. At the Zn K-edge only minor differences are observed in the FT EXAFS spectra suggesting a similar bonding environment. This is supported by the XANES region where only minor differences are observed attributable to changes in ligand orientation.[8] Overall the spectra exhibit features similar to the **ZIF-4** reference and consistent with the XRD data showing that a tetrahedral Zn environment is maintained throughout the treatment cycle.

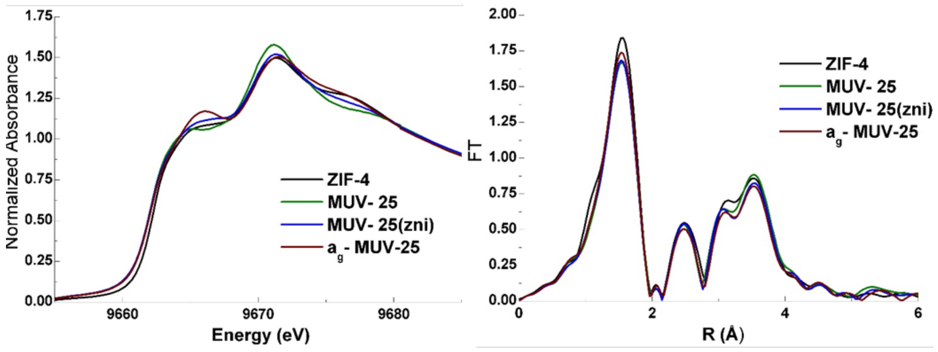

Figure S23. (left) XANES spectra at the Zn K-edge. (right) k^2-weighted Fourier Transformed Zn K-edge EXAFS. EXAFS were extracted using the autobk algorithm with E0 as the maximum of the first derivative employing an Rbkg of 1.1 over a k-range of 1–16.9 Å^{-1}. The EXAFS were Fourier transformed using a Hanning window over a k-range of 1–16 Å^{-1}.

On the other hand, marked differences are observed at the Fe K-edge. The **MUV-25(mog)** parent compound exhibits a pre-edge due to 1s→3d transitions centered at 7113.1 eV with an intensity of 0.06 normalized units (Figure S24, Table S5), strongly indicating the presence of a six coordinate Fe(II) center,[9,10] and consistent with EXAFS analysis and XRD data (Figure S25 and Table S6). Upon treatment, formation of **MUV-25(zni)** results in a marked increase in the pre-edge intensity consistent with the presence of a tetrahedral Fe(II) center. Upon further heating to 538 ºC **a$_g$-MUV-25** shows a ~1 eV shift in the pre-edge intensity consistent with oxidation of the iron center. Furthermore, the intensity of 0.17 is consistent with an average tetrahedral geometry but from EXAFS analysis formation of minor iron-oxides is also indicated by scattering paths Fe–C/N/O at 1.88 Å and Fe–Fe scattering at 3.68 Å.

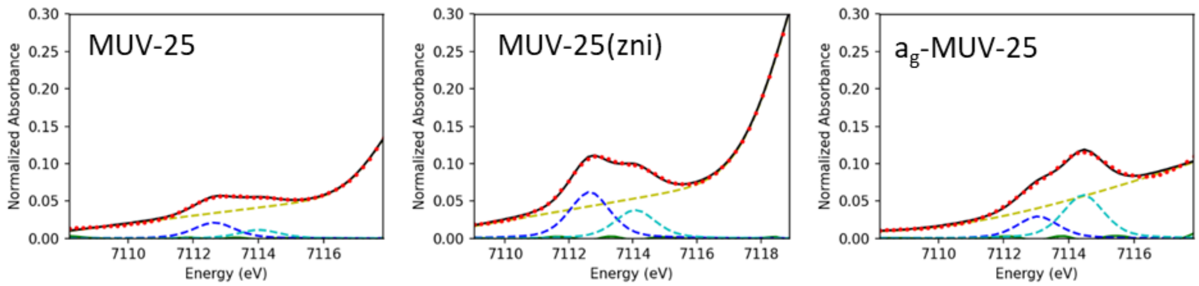

Figure S24. Fe K-edge pre-edge fits.

Table S5. Results of Fe K-edge pre-edge fits.

	Pre-edge (peak 1)		Pre-edge (peak 2)			
SAMPLE	**Energy (eV)**	**Intensity (norm.units)**	**Energy (eV)**	**Intensity (norm.units)**	**Total intensity (norm.units)**	**Pre-edge Energy (eV)***
MUV-25	7112.65(3)	0.04(0)	7114.03(7)	0.02(0)	0.06	7113.1
MUV-25(zni)	7112.65(1)	0.12(0)	7114.07(3)	0.07(0)	0.19	7113.2
a_g-MUV-25	7113.17(5)	0.06(0)	7114.51(6)	0.11(0)	0.17	7114.1

* The pre-edge energy is taken as the intensity weighted average.

Table S6. Fe K-edge: EXAFS were extracted with an R_{bkg} of 1 and a spline in the 0-15 Å^{-1} $k^{1,2,3}$-weighted fits carried out in r-space over a k-range of 3–12 Å using a Hanning window (dk 1), and an $S_0 = 0.9$ was chosen. Bond distances and disorder parameters (Δr_{eff} and σ^2) were allowed to float having initial values of 0.0 Å and 0.003 Å^2 respectively, with a universal E_0 and $\Delta E_0 = 0$ eV. σ^2 values reported as x 10^3 Å^2

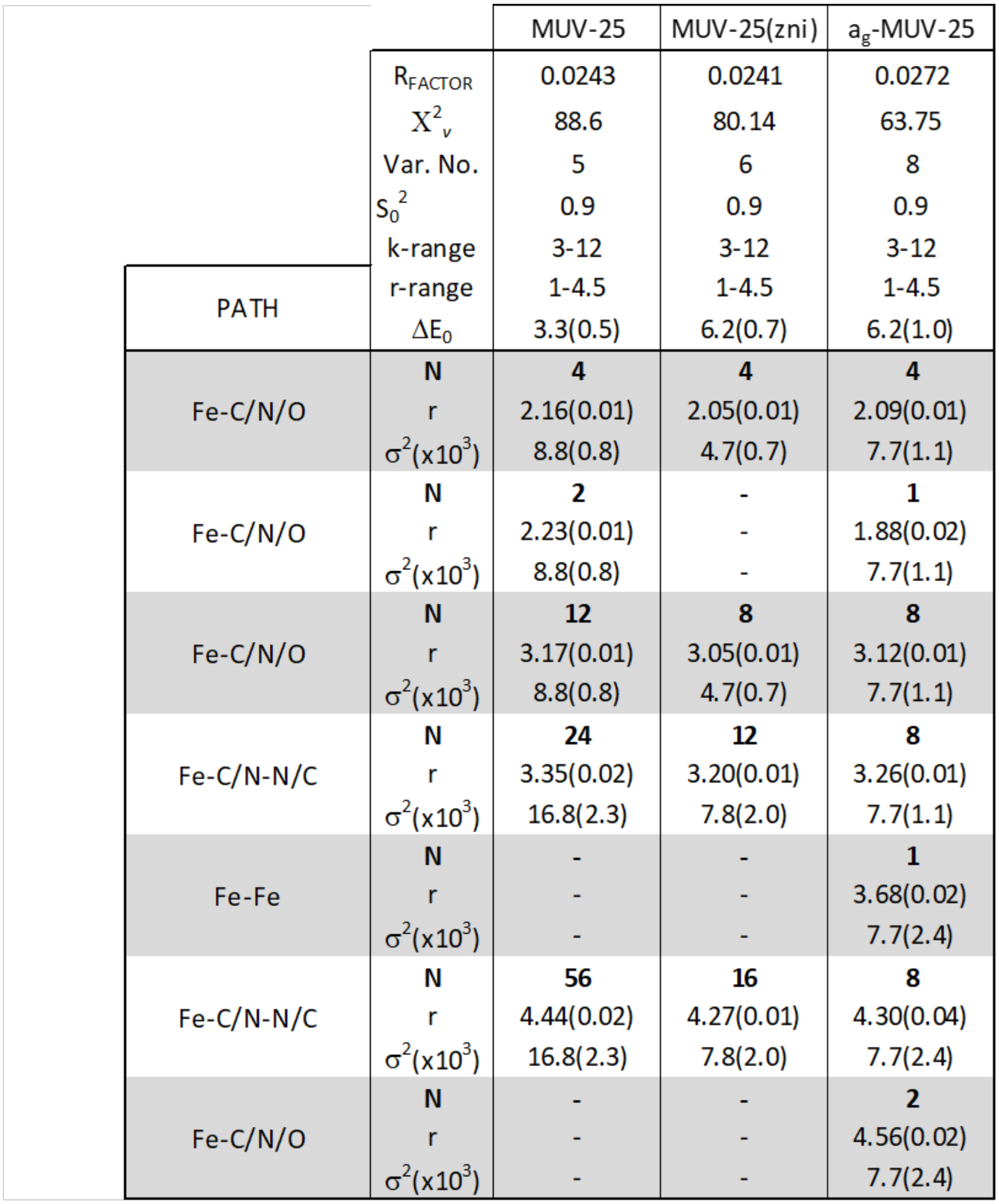

PATH		MUV-25	MUV-25(zni)	a_g-MUV-25
	R_{FACTOR}	0.0243	0.0241	0.0272
	X^2_v	88.6	80.14	63.75
	Var. No.	5	6	8
	S_0^2	0.9	0.9	0.9
	k-range	3-12	3-12	3-12
	r-range	1-4.5	1-4.5	1-4.5
	ΔE_0	3.3(0.5)	6.2(0.7)	6.2(1.0)
Fe-C/N/O	**N**	**4**	**4**	**4**
	r	2.16(0.01)	2.05(0.01)	2.09(0.01)
	$\sigma^2(x10^3)$	8.8(0.8)	4.7(0.7)	7.7(1.1)
Fe-C/N/O	**N**	**2**	**-**	**1**
	r	2.23(0.01)	-	1.88(0.02)
	$\sigma^2(x10^3)$	8.8(0.8)	-	7.7(1.1)
Fe-C/N/O	**N**	**12**	**8**	**8**
	r	3.17(0.01)	3.05(0.01)	3.12(0.01)
	$\sigma^2(x10^3)$	8.8(0.8)	4.7(0.7)	7.7(1.1)
Fe-C/N-N/C	**N**	**24**	**12**	**8**
	r	3.35(0.02)	3.20(0.01)	3.26(0.01)
	$\sigma^2(x10^3)$	16.8(2.3)	7.8(2.0)	7.7(1.1)
Fe-Fe	**N**	**-**	**-**	**1**
	r	-	-	3.68(0.02)
	$\sigma^2(x10^3)$	-	-	7.7(2.4)
Fe-C/N-N/C	**N**	**56**	**16**	**8**
	r	4.44(0.02)	4.27(0.01)	4.30(0.04)
	$\sigma^2(x10^3)$	16.8(2.3)	7.8(2.0)	7.7(2.4)
Fe-C/N/O	**N**	**-**	**-**	**2**
	r	-	-	4.56(0.02)
	$\sigma^2(x10^3)$	-	-	7.7(2.4)

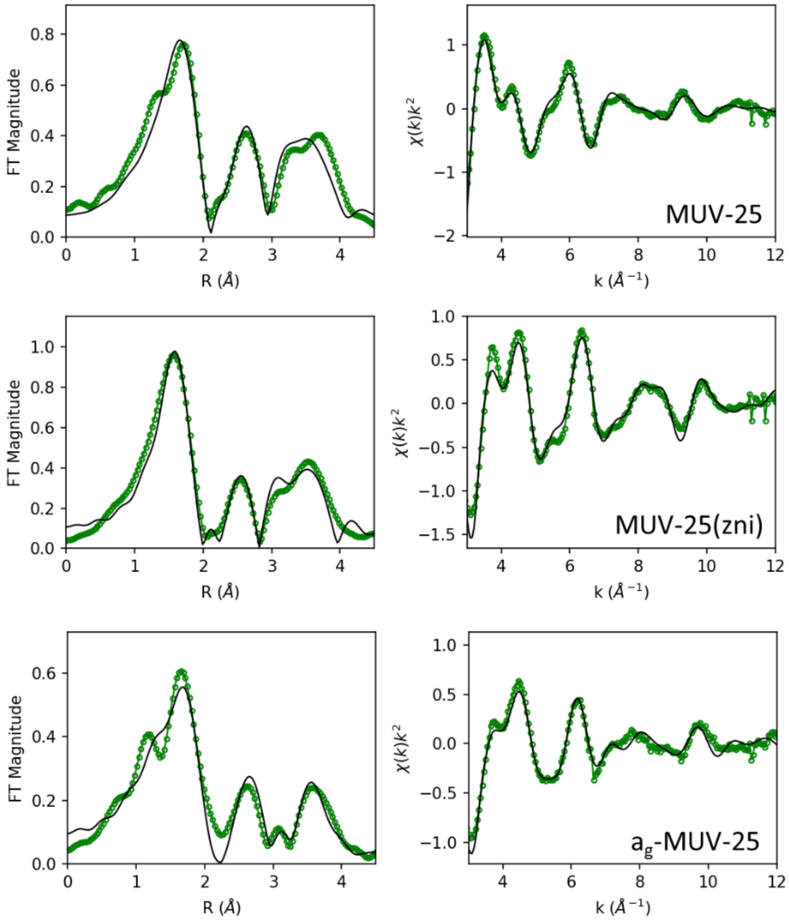

Figure S25. Fe K-edge EXAFS fits from Table S6.

S6. Scanning electron microscopy (SEM) and energy dispersive X-ray spectroscopy (EDX)

Scanning electron micrograph images were captured using the SCIOS 2 FIB-SEM. Samples were prepared by placing the powder on a carbon tape support and undergoing metallization before image collection. EDX analysis was conducted to examine the distribution of each metal ion within the crystal structure. The synthesis conditions of the materials were established previously using DSC equipment.

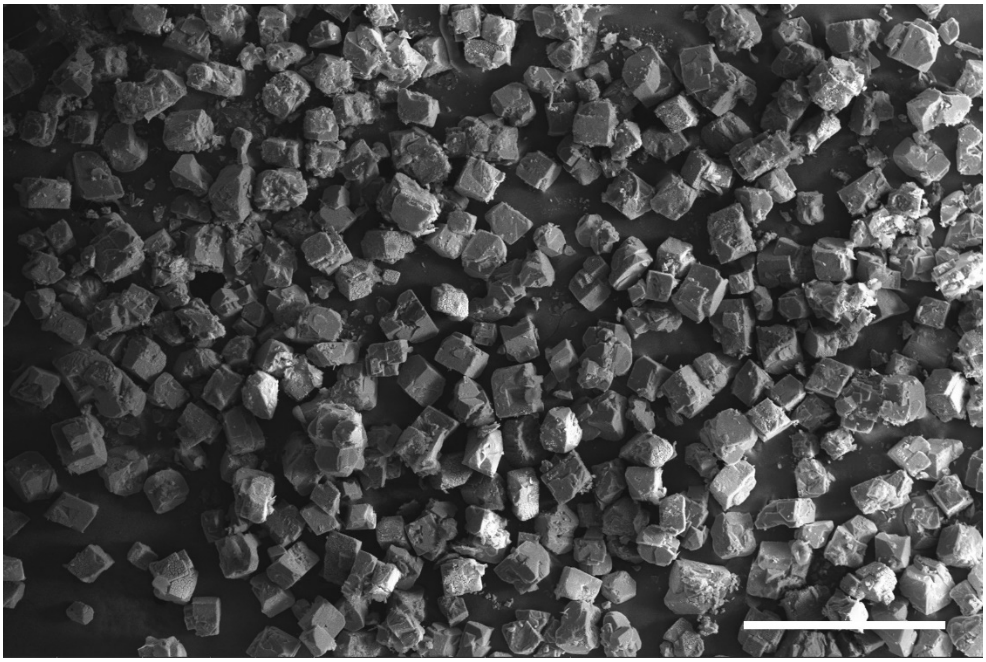

Figure S26. SEM image of **MUV-25(mog)** crystals. SEM scale bar is 500 µm.

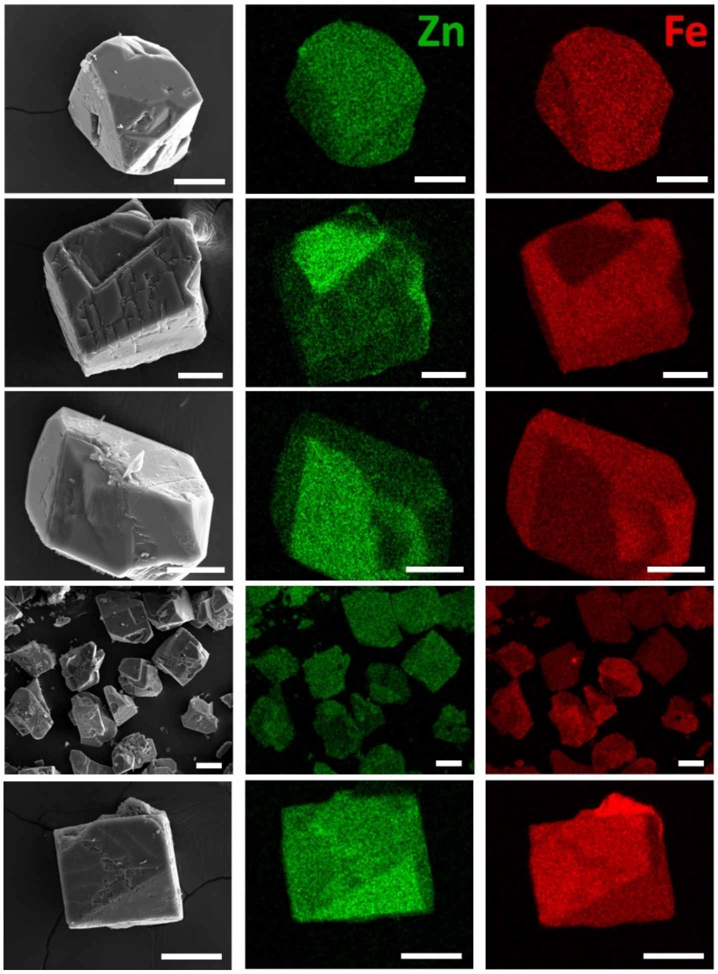

Figure S27. SEM and EDX mapping were performed on various crystals of **MUV-25(mog)**. The different distribution of the metal ions can be observed depending on the crystallographic phase. SEM scale bars are 50 μm.

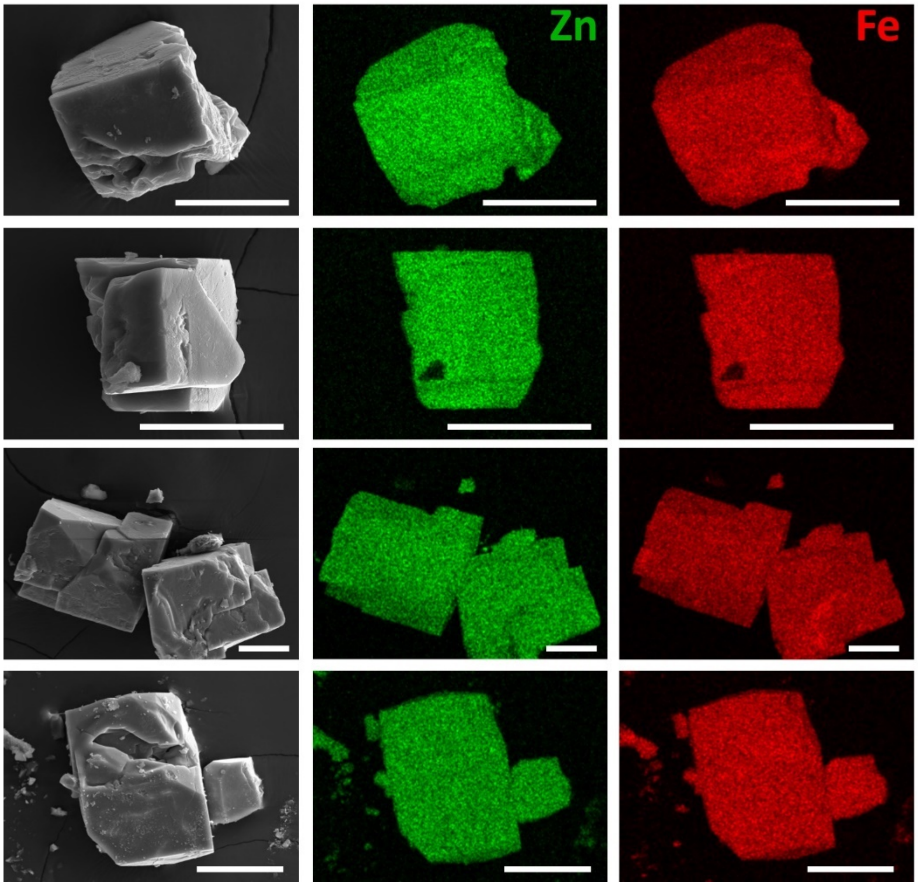

Figure S28. SEM and EDX mapping were performed on various crystals of **MUV-25(zni)**. A homogeneous distribution of the metal ions can be observed. SEM scale bars are 50 μm.

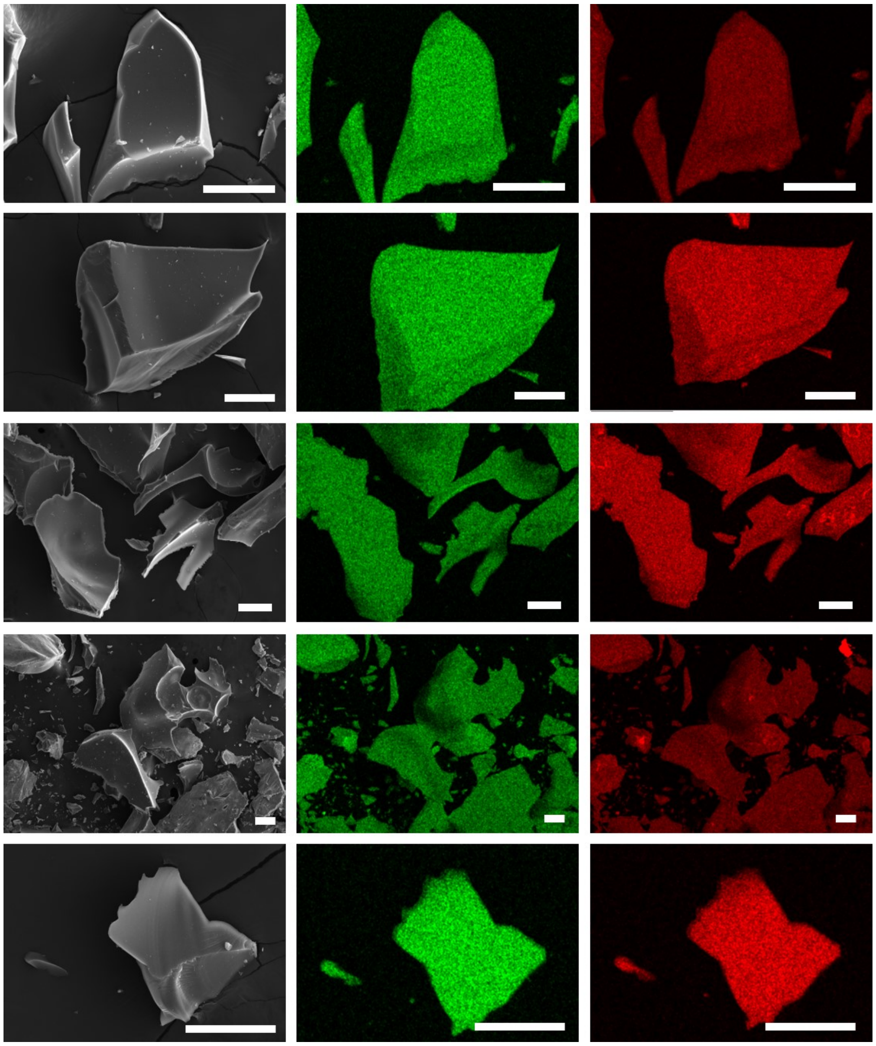

Figure S29. SEM and EDX mapping were performed on various crystals of **a_g-MUV-25**. A homogeneous distribution of the metal ions can be observed, along with a more monolithic phase. SEM scale bars are 50 μm.

S7. Inductively coupled plasma mass spectrometry (ICP-MS)

The chemical identity of each the different materials was confirmed by inductively coupled plasma mass spectrometry (ICP-MS), using an Agilent model 7900. The samples were subjected to a digestion process in a microwave oven.

Table S7. Quantity of individual metal ions within the various heterometallic materials prepared with different initial precursors. Note that these synthetic conditions yield mixtures of phases (see Figure S4 above).

Initial precursors	% Zn	% Fe
75Zn-25Fe	83.53	16.47
50Zn-50Fe (MUV-25)	66.42	33.58
25Zn-75Fe	43.72	56.28

Table S8. Quantity of individual metal ions within the different **MUV-25** phases.

Initial precursors	% Zn	% Fe
MUV-25(mog)	66.42	33.58
MUV-25(zni)	63.89	36.11
a_g-MUV-25	66.04	33.96

S8. Differential scanning calorimetry (DSC)

Differential Scanning Calorimetry (DSC) measurements were conducted using a DSC 250 instrument from TA Instruments. Approximately 10-15 mg of activated sample was loaded into an aluminum crucible (30 µL) with a pierced lid, while an empty aluminum crucible served as a reference. The sample, under a nitrogen gas atmosphere, was initially heated to 40 ºC, and an isotherm was held for 15 minutes to stabilize the sample. Subsequently, it was heated to its melting temperature at a rate of 10 ºC·min^{-1}.

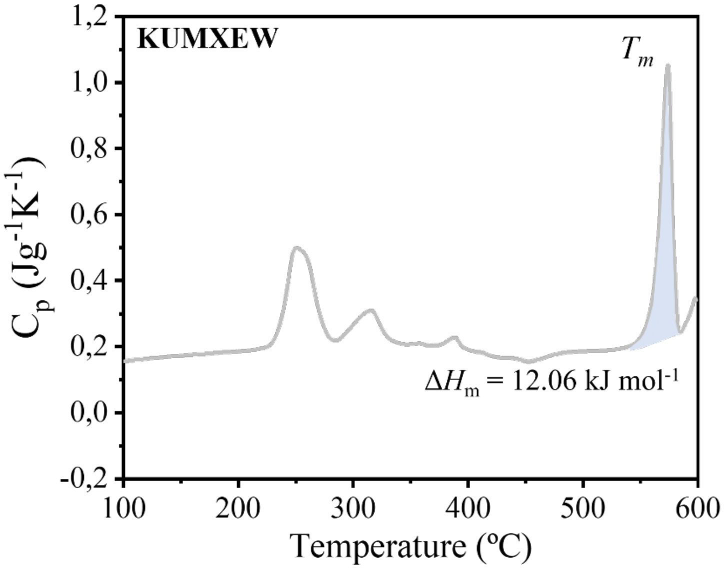

Figure S30. DSC measurement was conducted on **KUMXEW** at a heating rate of 10 ºC min^{-1}. The area under the endothermic peak corresponding to melting was integrated to determine the enthalpy.

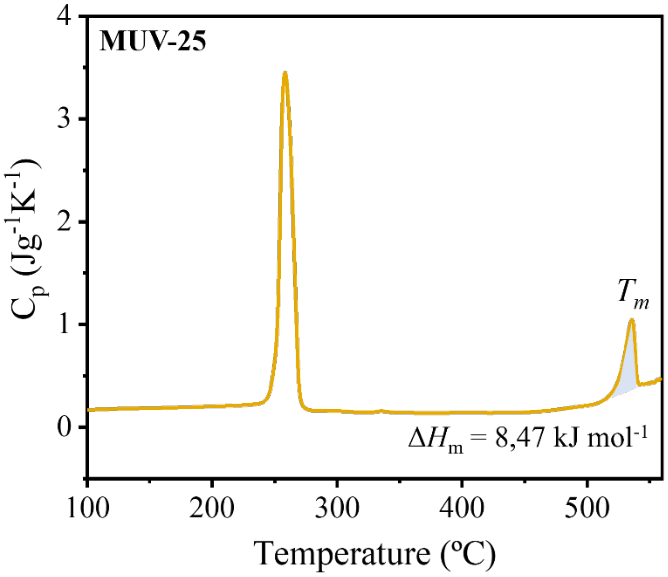

Figure S31. DSC measurement was conducted on **MUV-25** at a heating rate of 10 ºC min^{-1}. The area under the endothermic peak corresponding to melting was integrated to determine the enthalpy.

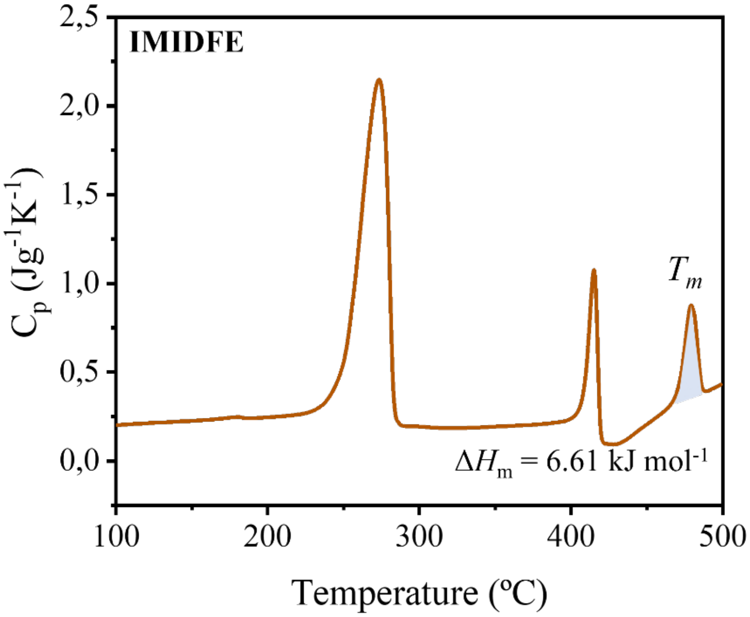

Figure S32. DSC measurement was conducted on **IMIDFE** at a heating rate of 10 ºC min^{-1}. The area under the endothermic peak corresponding to melting was integrated to determine the enthalpy.

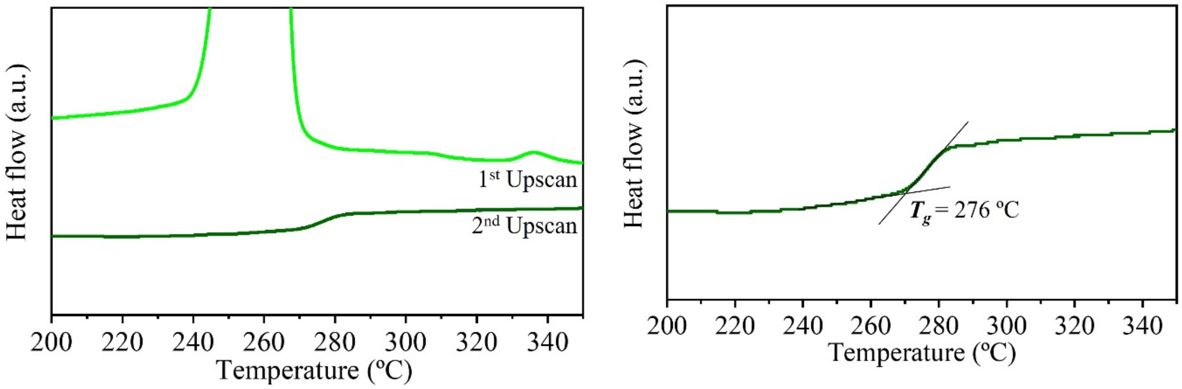

Figure S33. Successive DSC upscans of **MUV-25** reveal the appearance of a small step at 276 ºC at the second upscan, corresponding to the glass transition (T_g).

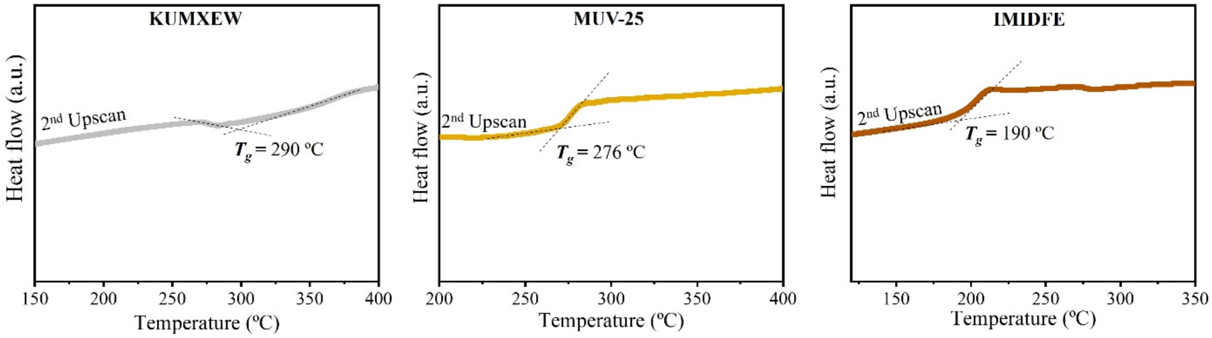

Figure S34. DSC second upscans of **KUMXEW**, **MUV-25**, and **IMIDFE** at a rate of 10 ºC min^{-1}, highlighting the glass transition.

S9. Liquid fragility measurements

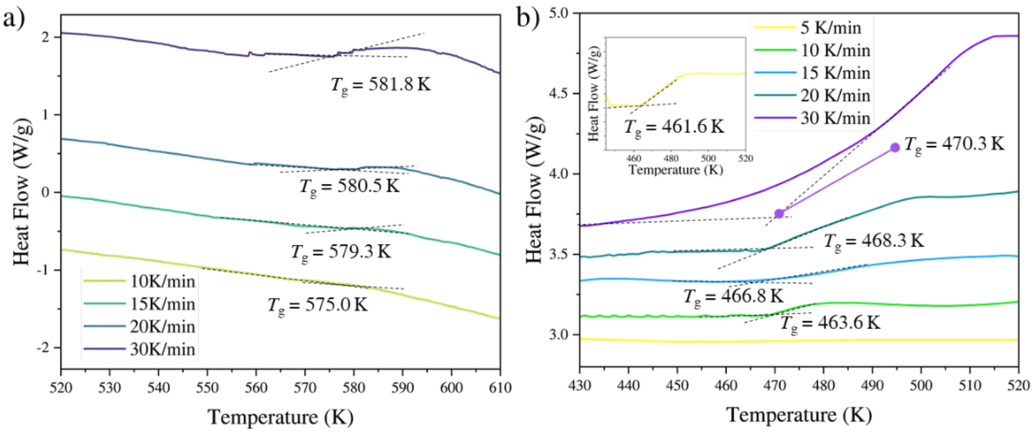

Figure S35. DSC measurements using different heating ratios for (a) **a$_g$-MUV-25** and (b) **a$_g$-MUV-24.**

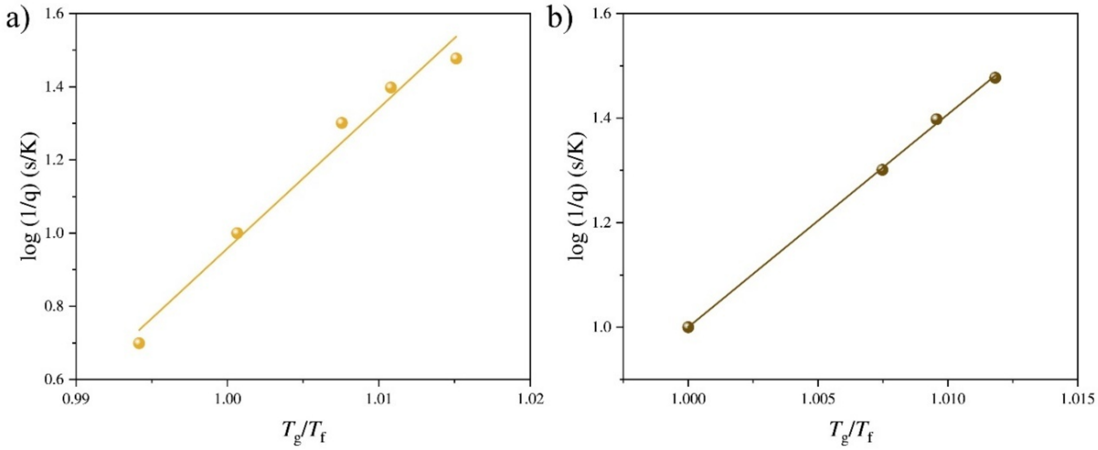

Figure S36. Linear fits of the fragility of the liquid (m) using equation 1 in the main text for (a) **a$_g$-MUV-25** and (b) **a$_g$-MUV-24**.

Table S9. Details from the fitting of the liquid fragility measurements.

Material	Intercept	Slope (Fragility, m)	Residual Sum of squares	R-square
a$_g$-MUV-25	-37.32 ± 3.26	38.30 ± 3.24	8.72E-3	0.97895
a$_g$-MUV-24	-39.70 ± 0.81	40.70 ± 0.80	1.03E-4	0.99921

S10. Nuclear magnetic resonance (NMR)

NMR spectra were recorded on a Bruker DRX-500 spectrometer. The ligand integrity was confirmed by ^{1}H NMR spectroscopy (upon digestion in D_2O and 3 drops of deuterated trifluoroacetic acid or deuterated sulfuric acid).

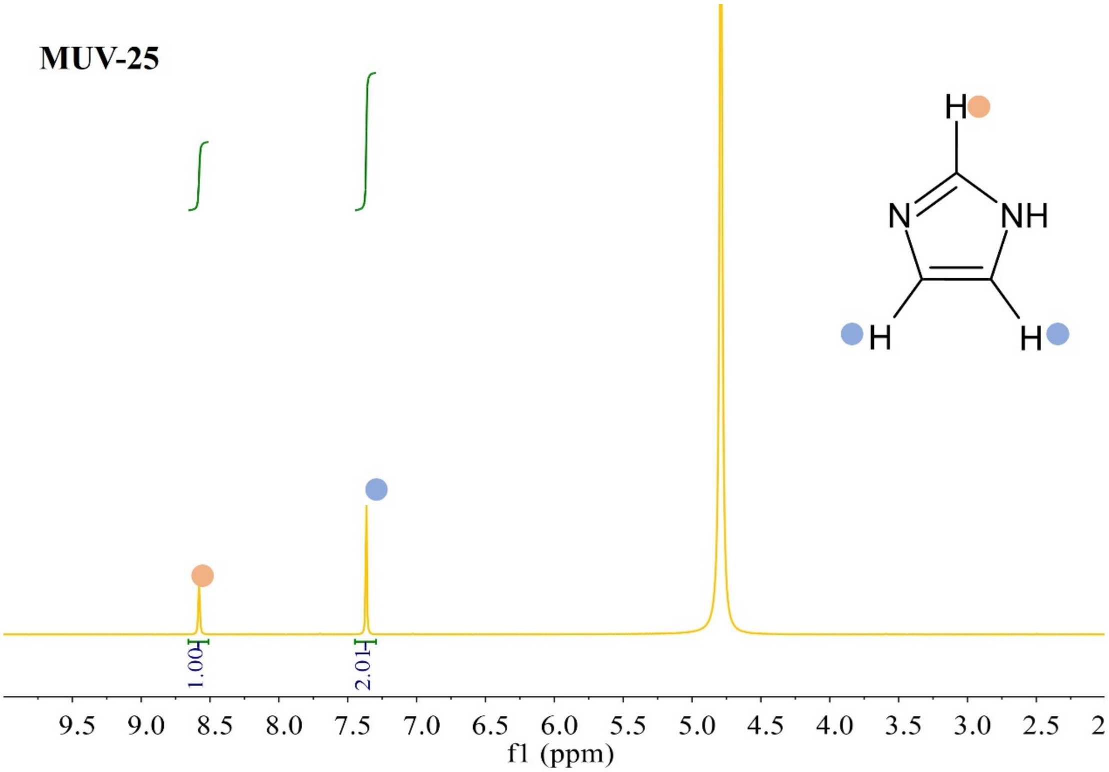

Figure S37. ^{1}H NMR spectra of digested **MUV-25(mog)** clearly illustrates the hydrogen atoms from the imidazole ligand. Colored circles represent the protons associated with each signal.

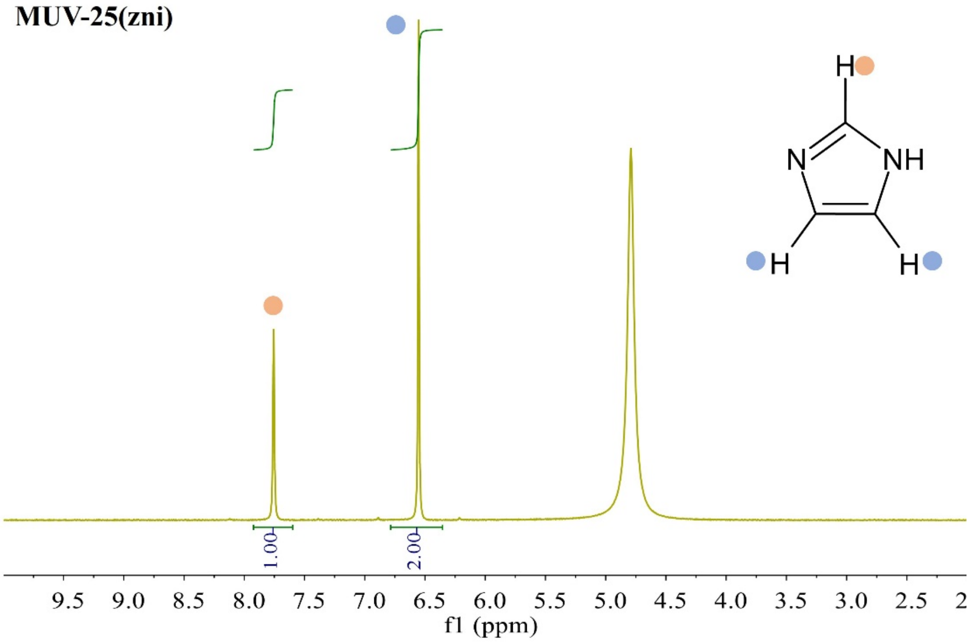

Figure S38. ^{1}H NMR spectra of digested **MUV-25(zni)** clearly illustrates the hydrogen atoms from the imidazole ligand. Colored circles represent the protons associated with each signal.

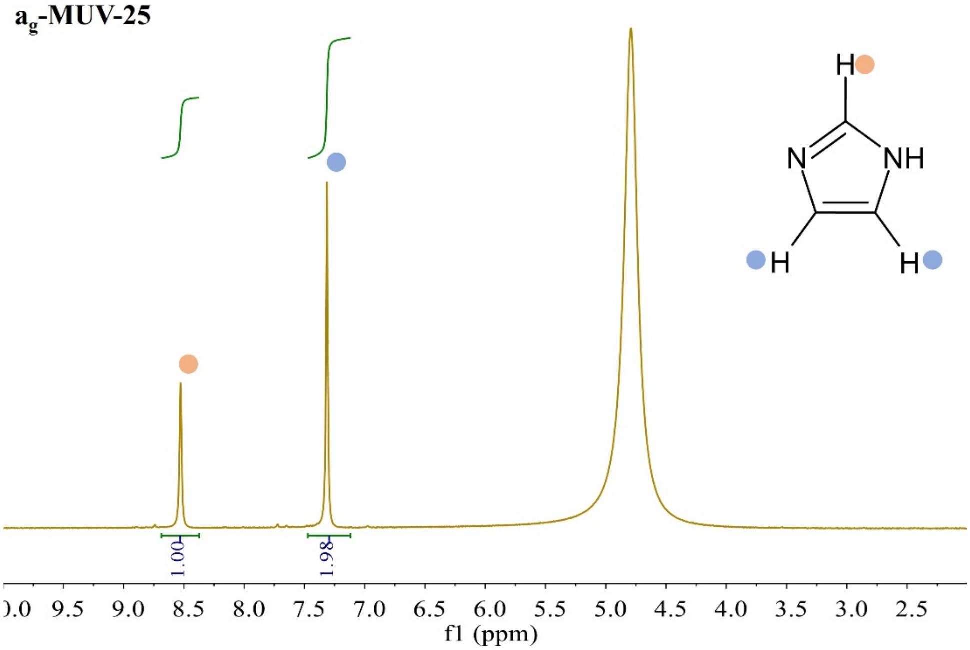

Figure S39. ^{1}H NMR spectra of digested **a_g-MUV-25** clearly illustrates the hydrogen atoms from the imidazole ligand. Colored circles represent the protons associated with each signal.

S11. Polarized light microscopy

Optical images were obtained with Nikin Eclipse LV-100 Optical microscope. Pictures of one **MUV-25(mog)**, **MUV-25(zni)** and **a$_g$-MUV-25** are reported.

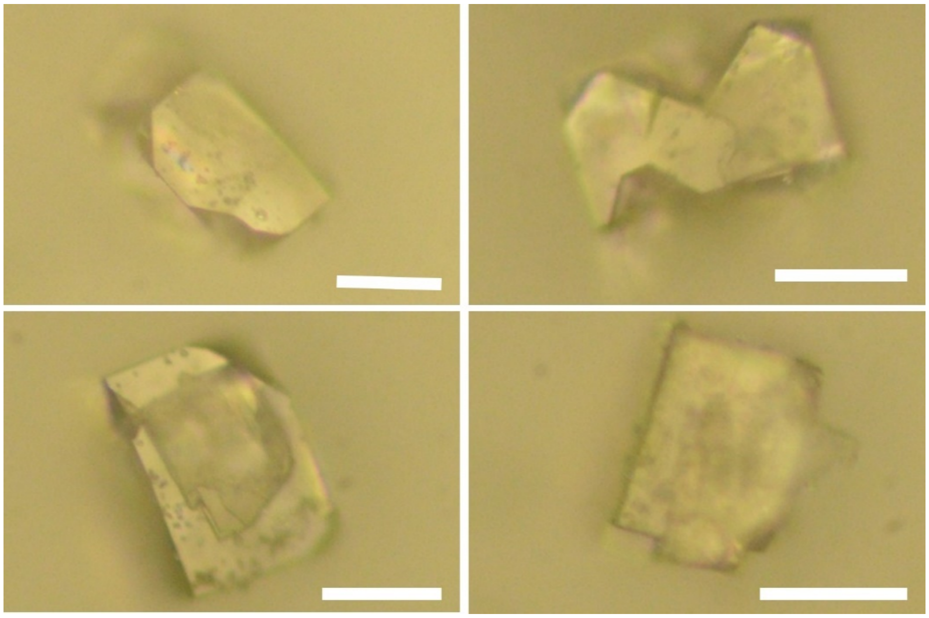

Figure S40. Optical images of different **MUV-25(mog)** crystals. Optical scale bars are 50 µm.

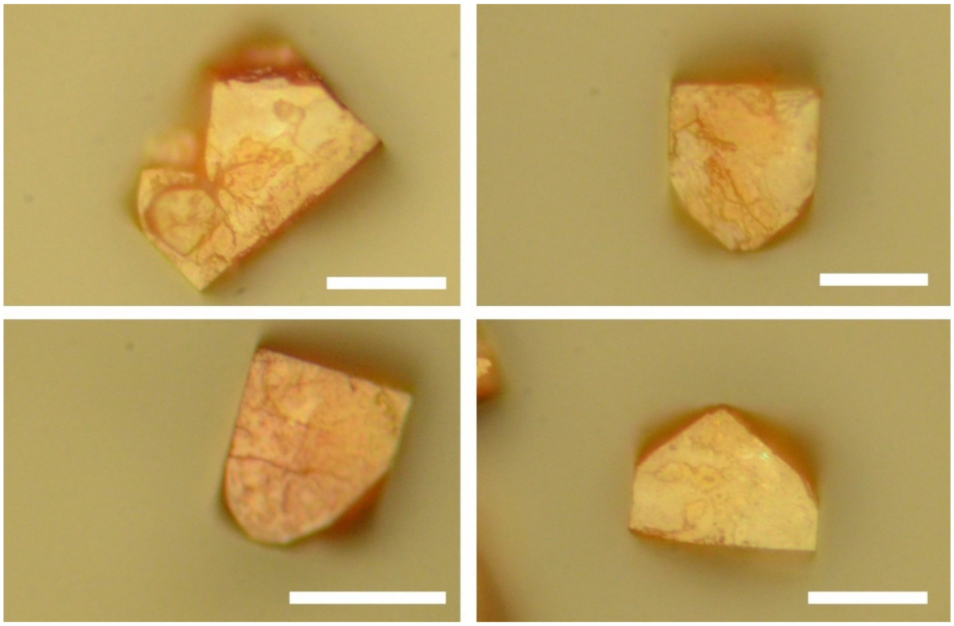

Figure S41. Optical images of different **MUV-25(zni)** crystals. Optical scale bars are 50 µm.

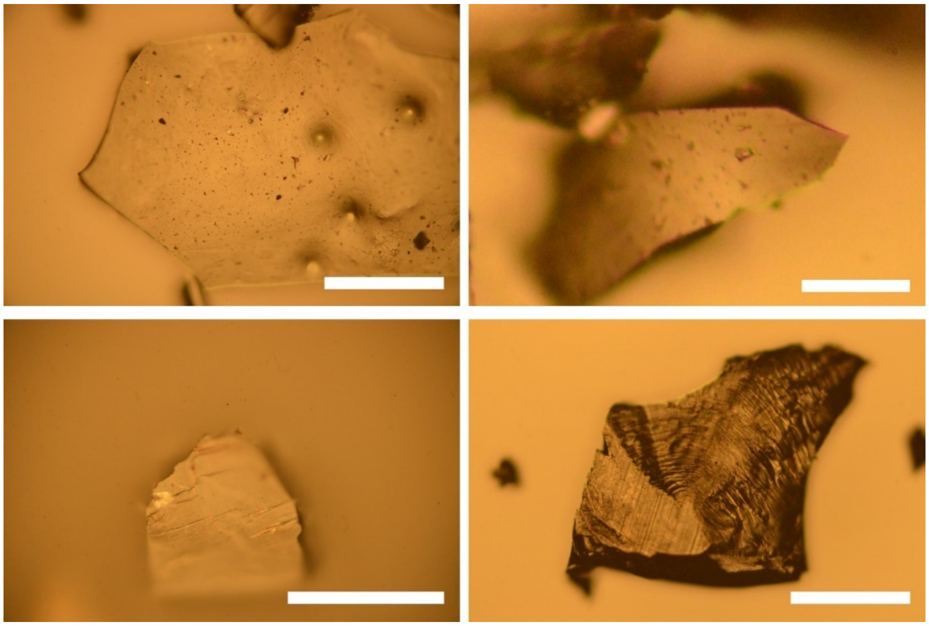

Figure S42. Optical images of different **a_g-MUV-25** monolithic glass. Optical scale bars are 50 μm.

S12. Infrared spectroscopy

Infrared spectra were registered using ALPHA II FTIR spectrometer (Bruker).

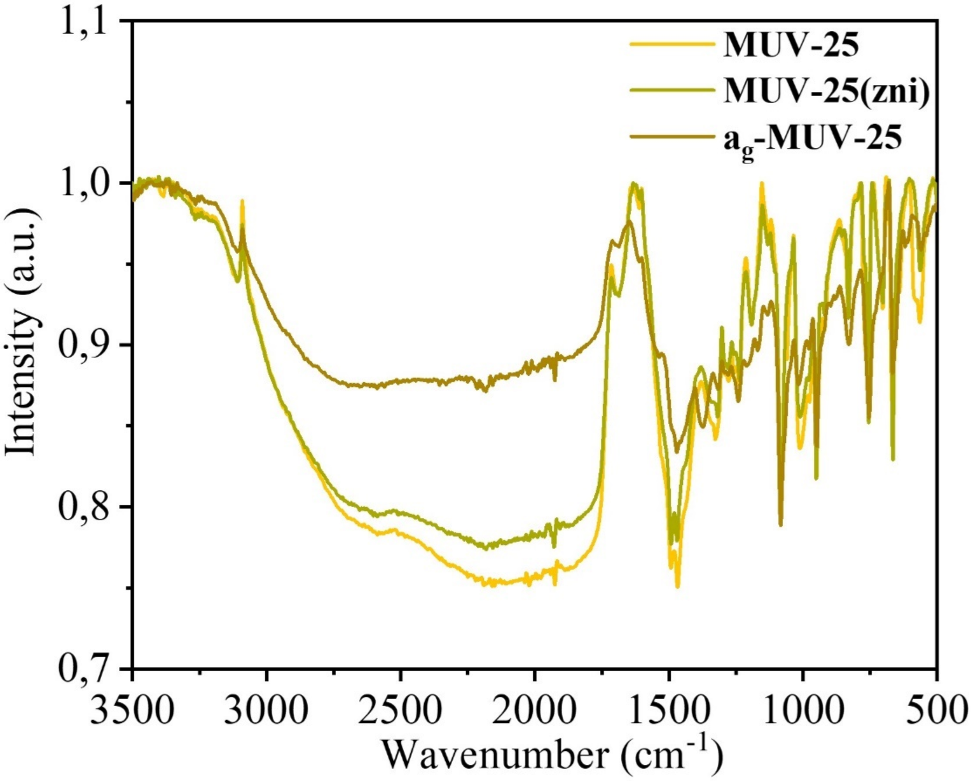

Figure S43. IR spectra of the different phases of **MUV-25**.

S13. References

(1) Sheldrick, G. M. SHELXT − Integrated space-group and crystal-structure determination. *Acta Cryst.* **2015**, *71*, 3−8.

(2) Dolomanov, O. V.; Bourhis, L. J.; Gildea, R. J.; Howard, J. A. K.; Puschmann, H. OLEX2: A Complete Structure Solution, Refinement and Analysis Program. *J. Appl. Crystallogr.* **2009**, *42*, 339−341.

(3) Soper, A. K.; Barney, E. R. Extracting the Pair Distribution Function from White-Beam X-Ray Total Scattering Data. *J. Appl. Crystallogr.* **2011**, *44*, 714–726.

(4) Soper, A. GudrunN and GudrunX : Programs for Correcting Raw Neutron and X-Ray Diffraction Data to Differential Scattering Cross Section. *Rutherford Appleton Laboratory Technical Reports* **2011**.

(5) Keen, D. A. A Comparison of Various Commonly Used Correlation Functions for Describing Total Scattering. *J. Appl. Crystallogr.* **2001**, *34*, 172–177.

(6) Juhás, P.; Farrow, C. L.; Yang, X.; Knox, K. R.; Billinge, S. J. L. Complex Modeling: A Strategy and Software Program for Combining Multiple Information Sources to Solve Ill Posed Structure and Nanostructure Inverse Problems. *Acta Crystallogr. A Found. Adv.* **2015**, *71*, 562–568.

(7) Crystallographic Open Database ID:1010369

(8) Boada, R.; Chaboy, J. J.; Hayama, S.; Keenan, L. L.; Freeman, A. A.; Amboage, M.; Díaz-Moreno, S. Unraveling the Molecular Details of the “Gate Opening” Phenomenon in ZIF-8 with X-Ray Absorption Spectroscopy. *J. Phys. Chem. C* **2022**, *126*, 5935–5943.

(9) Chandrasekaran, P.; Stieber, S. C. E.; Collins, T. J.; Que, L.; Neese, F.; Debeer, S. Prediction of High-Valent Iron K-Edge Absorption Spectra by Time-Dependent Density Functional Theory. *Dalt. Trans.* **2011**, *40*, 11070–11079.

(10) Westre, T. E.; Kennepohl, P.; DeWitt, J. G.; Hedman, B.; Hodgson, K. O.; Solomon, E. I. A Multiplet Analysis of Fe K-Edge 1s → 3d Pre-Edge Features of Iron Complexes. *J. Am. Chem. Soc.* **1997**, *119*, 6297–6314.